Lithos 216–217 (2015) 1–16

Contents lists available at ScienceDirect

Lithos

journal homepage: www.elsevier.com/locate/lithos

Orthopyroxene–omphacite- and garnet–omphacite-bearing magmatic assemblages, Breaksea Orthogneiss, New Zealand: Oxidation state controlled by high-*P* oxide fractionation ☆

Timothy Chapman [a,*], Geoffrey L. Clarke [a], Nathan R. Daczko [b,c], Sandra Piazolo [b,c], Adrianna Rajkumar [a]

[a] School of Geosciences, F09, University of Sydney, Sydney, NSW 2006, Australia
[b] ARC Centre of Excellence for Core to Crust Fluid Systems, Department of Earth and Planetary Sciences, Macquarie University, NSW 2109, Australia
[c] GEMOC, Department of Earth and Planetary Sciences, Macquarie University, NSW 2109, Australia

ARTICLE INFO

Article history:
Received 19 December 2013
Accepted 21 November 2014
Available online 3 December 2014

Keywords:
Omphacite–garnet granulite
Orthopyroxene eclogite
Omphacite–orthopyroxene granulite
REE
Igneous omphacite
EBSD microstructure

ABSTRACT

The Breaksea Orthogneiss comprises a monzodioritic host partially recrystallised to omphacite–garnet–plagioclase–rutile granulite at 850 °C and 1.8 GPa, with metre to decametre-scale, cognate inclusions ranging from ultramafic through gabbroic to monzodioritic composition. Coarsely layered garnetite and diopsidic clinopyroxenite cumulate preserves igneous textures, whereas garnet–omphacite cumulate shows a partial metamorphic overprint to eclogite. Garnet and omphacite in undeformed to weakly deformed rocks have similar major and rare earth element characteristics reflecting their common igneous origin, pointing to a lack of metamorphic recrystallisation. Inclusions of omphacite–orthopyroxene–plagioclase–ulvöspinel orthogneiss have whole-rock compositions almost identical to the host monzodiorite. Reaction zones developed along contacts between the orthopyroxene-bearing inclusions and host contain metamorphic garnet that is microstructurally and chemically distinct from igneous garnet. The presence of orthopyroxene is interpreted to reflect redox distinctions: early, oxidised magma crystallised orthopyroxene and ulvöspinel at high-*P* (~1.8 GPa), garnet crystallisation having been suppressed. Progressive fractionation of oxygen into early formed phases (ulvöspinel, magnetite, orthopyroxene, ferric iron-rich omphacite and rare garnet) drove the magma to less oxidising conditions, resulting in the more common igneous assemblage of garnet, omphacite and rutile in the main host.

1. Introduction

The lower crustal roots of magmatic arcs are exposed in only a few locations, such as the Ladakh–Kohistan arc in Northern Pakistan (Jagoutz and Schmidt, 2012), the Talkeetna arc in Alaska (Behn and Keleman, 2006; DeBari and Coleman, 1989) and the Fiordland arc, New Zealand (Clarke et al., 2000; Daczko et al., 2009, 2012). Crustal thicknesses inferred commonly for magmatic arcs lie in the range of 30 to 40 km (1.0–1.4 GPa at their base), with some overthickened Cordilleran arcs reaching thicknesses in excess of 50 km (1.5–2.0 GPa). At such deep crustal levels, intermediate to mafic high-*P* granulite and eclogite are predicted to be the dominant rock types (O'Brien and Rötzler, 2003; Rudnick and Fountain, 1995). These rare exposures provide unique insights into the dynamics of lower crustal processes, in particular the interplay between magmatic and metamorphic processes, that otherwise can only be directly observed *via* xenoliths (*e.g.* Griffin et al., 1979).

There are large overlaps in the stability of mineral assemblages commonly occurring in high-grade orthogneisses and their plutonic protoliths. This commonality can lead to ambiguity in distinguishing metamorphic grains from igneous relicts, and debate concerning petrologic and tectonic interpretations of lower continental crustal rocks (*e.g.* Kotková and Harley, 2010; Štípská and Powell, 2005; Williams et al., 2000). The Cretaceous Breaksea Orthogneiss in Fiordland (De Paoli et al., 2012) presents such an example, incorporating rare exposures of intermediate to mafic lower crustal rocks formed in a thickened arc. Igneous crystallisation and subsequent metamorphic recrystallisation at high-*P* and high-*T* produced omphacite–garnet–plagioclase assemblages in monzodioritic compositions, and eclogite facies assemblages in gabbroic compositions (De Paoli et al., 2012). However, Clarke et al. (2013) interpreted that the majority of observed mineral assemblages in the Breaksea Orthogneiss should be attributed to igneous crystallisation, based on commonality in the rare earth element (REE) content of garnet and clinopyroxene across diverse cogenetic rock types.

Mineral assemblages involving orthopyroxene and omphacite occur in both granulite and eclogite components of the Breaksea Orthogneiss, presenting an unusual mix of minerals commonly considered characteristic of low- and high-*P* granulite facies conditions (*e.g.* De Paoli et al., 2012; Green, 1970; Green and Ringwood, 1967). Orthopyroxene–

☆ Mineral abbreviations given follow Kretz (1983).

* Corresponding author. Tel.: +61 2 93518199.
E-mail address: t.chapman@sydney.edu.au (T. Chapman).

http://dx.doi.org/10.1016/j.lithos.2014.11.019
0024-4937/

omphacite-bearing rocks have been reported from eclogite in the Western Gneiss Region, Norway (Mørk, 1985; Nakamura, 2003) and the Grenville Province, Canada (Indares, 1993), being attributed to high-Mg bulk rock compositions and/or metastable igneous orthopyroxene relicts. In contrast, the Breaksea Orthogneiss represents the first reported granulite with co-existing omphacite and orthopyroxene. This unusual mineral assemblage requires explanation in the context of phase stability and the nature of metamorphic and/or igneous origins related to lower crustal rocks (Clarke et al., 2013; Pattison, 2003; Racek et al., 2008; Ringuette et al., 1999; Štípská and Powell, 2005).

In this paper, we integrate field relationships and petrography with a detailed microstructural analysis of major and trace element mineral chemistry within orthopyroxene-bearing rocks to characterise igneous and metamorphic reaction histories that augment the work of Clarke et al. (2013). Combining these methods leads us to conclude that the presence, or absence of orthopyroxene reflects redox changes in the parent magma, which progressed from early comparatively oxidised conditions where orthopyroxene crystallised, to a later, more voluminous system at comparatively reduced conditions that stabilised the host assemblage of garnet, omphacite, plagioclase and rutile.

2. Geological setting and previous work

2.1. Geological setting

The Breaksea Orthogneiss (Allibone et al., 2009; De Paoli et al., 2009) is a high-*P* (1.8 GPa) component of the Western Fiordland Orthogneiss, a voluminous pulse of high-Sr/Y Early Cretaceous (125–115 Ma) arc magma emplaced inboard of the proto-Pacific Gondwana margin (Allibone and Tulloch, 2004; Bradshaw, 1989, 1993; Kimbrough et al., 1993, 1994; Mortimer et al., 1999; Muir et al., 1995, 1998). The Breaksea Orthogneiss is composite, mostly comprising an omphacite–garnet granulite host of monzodioritic composition (*c.* 60–65%), with layers and pods of peridotgabbroic eclogite (*c.* 25%: including both orthopyroxene-bearing and absent proportions), monzodioritic omphacite–orthopyroxene granulite (*c.* 5–10%), and minor garnetite, clinopyroxenite, harzburgite and hornblende peridotite (collectively *c.* 5%: Clarke et al., 2013). Primary compositional layering in granulite and eclogite are mostly transposed into an intense shallowly dipping gneissic foliation (De Paoli et al., 2009). Igneous protoliths were deformed and metamorphosed at $P \approx 1.8$ GPa and $T \approx 800$–850 °C in the root of the Fiordland arc (De Paoli et al., 2009, 2012). The shallow dipping Resolution Island Shear Zone (RISZ) forms an upper carapace to the Breaksea Orthogneiss, and juxtaposes it with Palaeozoic metasedimentary rocks of the Gondwana margin (Beltka and Klepeis, 2013; De Paoli et al., 2009). This study focuses on samples primarily collected distal to the RISZ, along a well exposed ridge transect between Breaksea Sound and Coal River informally referred to as the 'Breaksea Tops' and from the mouth of Breaksea Sound, where rare omphacite–orthopyroxene assemblages outcrop (Fig. 1a). Samples from Breaksea Sound show more effects of the RISZ and limited weathering related to their coastal exposure, with such effects minimised by selective sampling.

2.2. Igneous and metamorphic assemblages in the Breaksea Orthogneiss: previous work

Whole-rock analyses of eclogite and granulite at both Breaksea Tops and Breaksea Sound define a linear trend between monzodioritic and peridotgabbroic compositions (Fig. 1b: after De Paoli et al., 2009; Clarke et al., 2013). Contacts between centimetre- to decimetre-scale mafic pods or layers and the host granulite are gradational with varying proportions of garnet, clinopyroxene and plagioclase, a feature attributed to cumulate processes that preceded high-grade penetrative deformation (De Paoli et al., 2009). De Paoli et al. (2009) reported that mafic components preserve eclogite-facies garnet, omphacite and rutile with or without orthopyroxene. These are interlayered with metadioritic components with a granulite-facies assemblage involving garnet, omphacite, plagioclase, K-feldspar, rutile and kyanite. Clarke and co-workers subsequently distinguished two texturally distinct garnet forms in the granulite that reflect differing growth stages: igneous Type 1 garnet occurs as granoblastic grains in cm-scale mafic clusters with omphacite and sparsely distributed throughout the enclosing plagioclase-rich matrix; and metamorphic Type 2 garnet occurs as intergrowths with quartz, in coronate and necklace reaction structures separating clinopyroxene from plagioclase.

Garnet and clinopyroxene textures and mineral REE patterns in coarse-grained garnetite and clinopyroxenite components have been interpreted to record igneous growth stages, igneous microstructures and mineral compositions having persisted through high-grade metamorphism due to low strain, the comparatively slow intracrystalline diffusion of REE and limited major element mobility (Clarke et al., 2013). The clinopyroxenite and garnetite bodies have also been genetically linked to granulite and eclogite, based on garnet REE content (Clarke et al., 2013). The commonality in the REE patterns of idioblastic garnet and omphacite across all orthogneiss components (garnetite, clinopyroxenite, eclogite, granulite) has been used to argue that the garnetite, clinopyroxenite and eclogite bodies formed as cumulates from a common monzodioritic parent (Clarke et al., 2013).

Most granoblastic grain shapes in granulite and eclogite appear metamorphic, yet garnet mostly lacks a positive Eu anomaly that could be expected if it formed *via* plagioclase consuming metamorphic reactions at high-*P* conditions (De Paoli et al., 2012; Schröter et al., 2004). Pronounced overlap of mineral REE contents in garnetite and clinopyroxenite is consistent with an igneous origin for the majority of garnet, and thus also of omphacite in eclogite (garnet and clinopyroxene volumetrically encompass 90%) (Clarke et al., 2013). Igneous and metamorphic growth relationships of omphacite in granulite are less clear. Garnet has similar REE patterns to eclogite but distinct mineral associations and microstructures. Metamorphic garnet (Type 2) in granulite has a pronounced positive Eu anomaly, and subtly enriched grossular and diminished HREE content that distinguishes them from igneous Type 1 garnet (Clarke et al., 2013). Textural and geochemical relationships preserved in the Breaksea Orthogneiss are thus consistent with much of the gneiss retaining igneous porphyroclastic material. Neoblastic garnet (Type 2), attenuated omphacite, kyanite, clinozoisite and plagioclase in granulite components reflect metamorphic recrystallisation at $P = 1.8$–1.9 GPa and $T = 800$–850 °C (De Paoli et al., 2009, 2012) that accompanied the development of S2 and occurred shortly after pluton emplacement. Subjectively, the extent of metamorphic recrystallisation might be expected to reflect strain intensity, less pervasive in eclogite and best developed in granulite components (Clarke et al., 2013; De Paoli et al., 2009).

Clarke et al. (2013) concentrated on the origin of the host omphacite–garnet granulite, eclogite and interlayered garnetite and clinopyroxenite. However, the presence and/or absence of orthopyroxene in the Breaksea Orthogneiss has not been considered or discussed. The interpretation that mineral assemblages of the Breaksea Orthogneiss are dominantly of igneous origin, particularly omphacite, is still ambiguous in intermediate granulite components and warrants further testing (Clarke et al., 2013). Consequently, this study focuses on the orthopyroxene-bearing assemblages, establishing field, chemical and microstructural relationships to the other main components of the Breaksea Orthogneiss. In doing so, their petrological bearing on the lower crustal environment can be ascertained.

3. Field relationships and petrography

The Breaksea Orthogneiss has distinctive compositional mafic layering that occurs in places oblique to the dominant S_1 gneissic foliation (De Paoli et al., 2009). *Omphacite–orthopyroxene granulite* occurs as pods and discontinuous, centimetre- to decametre-layers cut by dykes/layers of omphacite–garnet granulite (Fig. 2a). The discontinuous, centimetre- to decimetre-scale mafic lenses and layers give much of

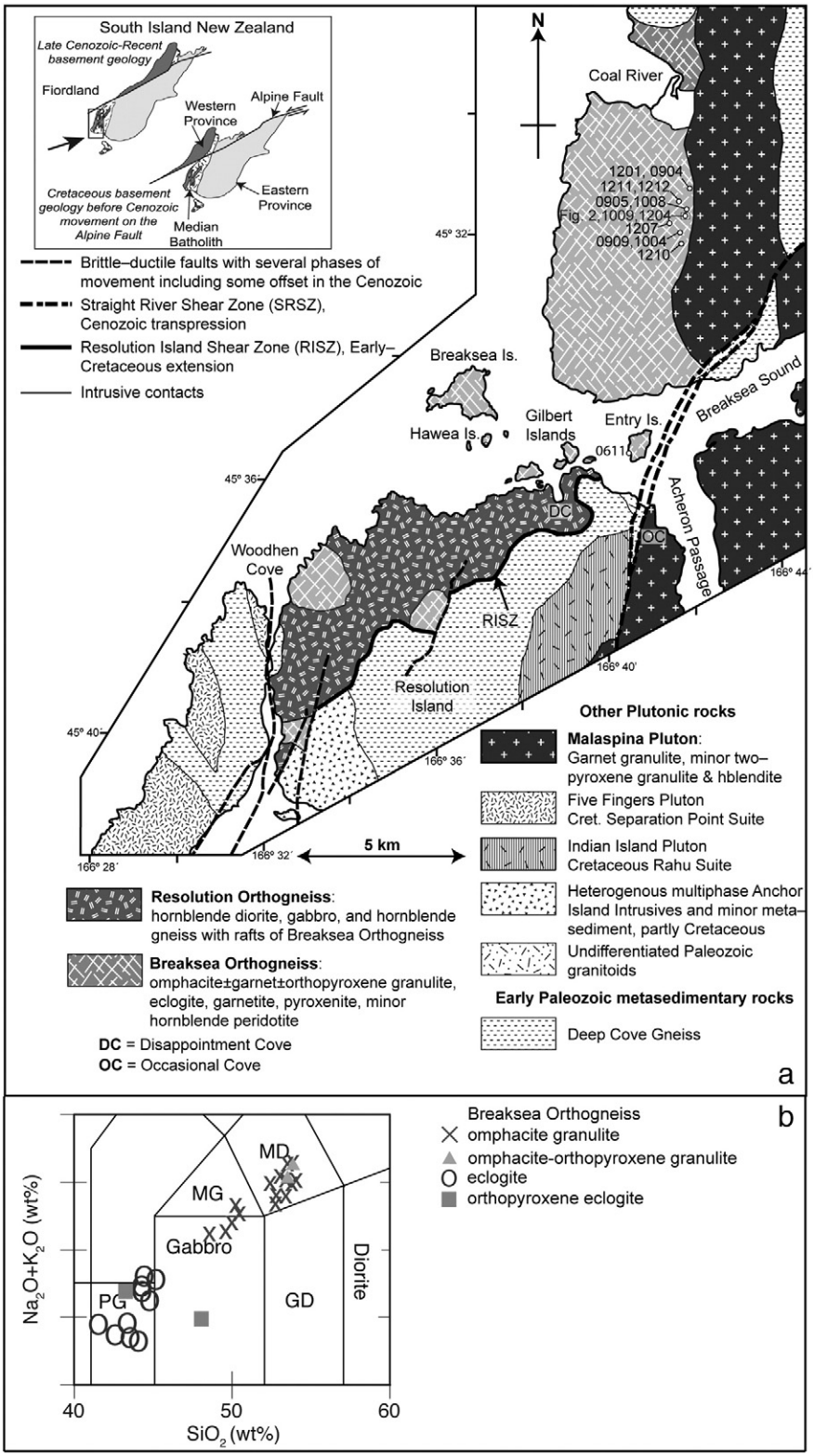

Fig. 1. a) Geological map of the Breaksea Sound area, between northern Resolution Island and Coal River (after Allibone et al., 2009). Paleozoic Takaka metasedimentary rocks form a structural carapace to Cretaceous orthogneisses beneath the RISZ. Numbered circles show sample locations used in this study. b) Modified total alkali–silica (TAS) plot for eclogite and granulite components of the Breaksea Orthogneiss after De Paoli et al. (2009) and Clarke et al. (2013), illustrating a general linear trend between peridotgabbroic and monzodioritic protoliths. TAS plots adapted for plutonic rocks after Middlemost (1994). PG = peridotgabbro; MG = monzogabbro; MD = monzodiorite; GD = gabbroic diorite.

the orthogneiss a distinctive patchy appearance. The omphacite–orthopyroxene granulite is separated from omphacite–garnet granulite by centimetre- to metre-scale *reaction zones* defined by abundant Type 2 garnet (Fig. 2a & c), though nebulitic contacts may be indistinct in field setting. Immediately adjacent to some omphacite–orthopyroxene granulite components are delicate layers of nearly pure omphacite 5–10 mm across, mantled by fine-grained Type 2 garnet (Fig. 2d). *Orthopyroxene eclogite* occurs as centimetre- to decametre-scale dykes and pods within

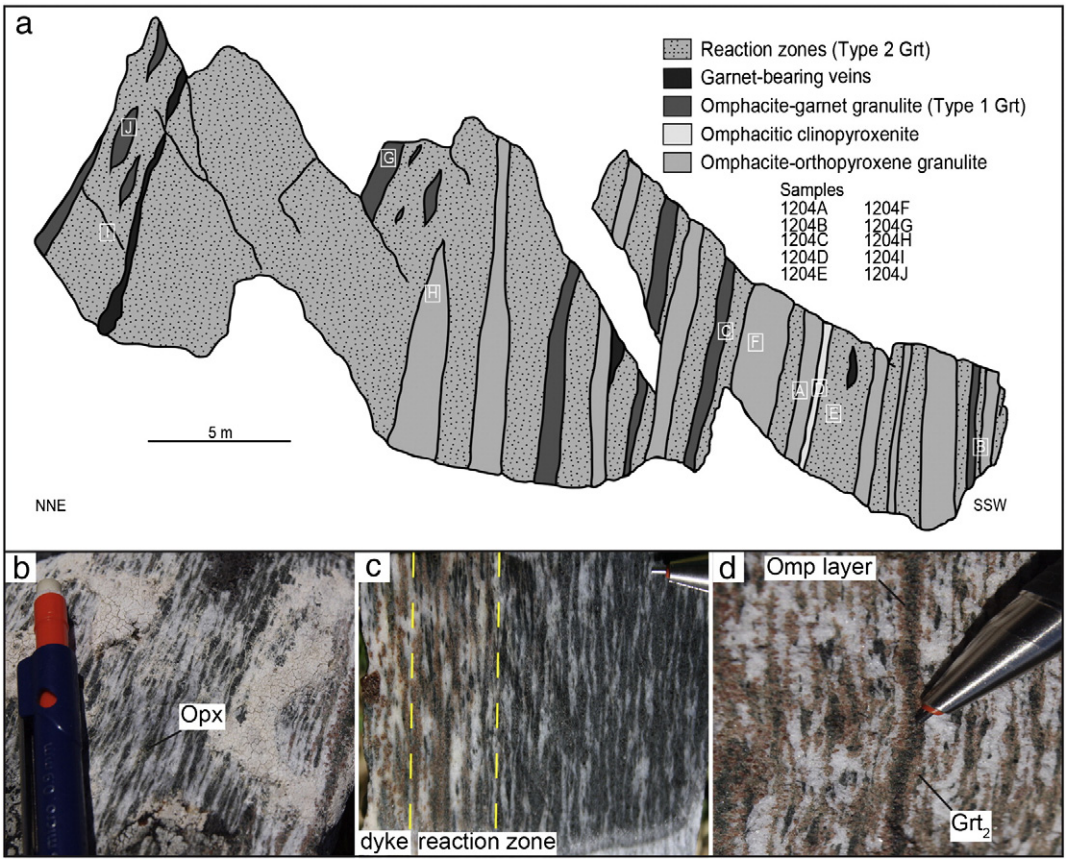

Fig. 2. a) Field relationships of granulite components at Breaksea Tops. The outcrop of monzodioritic omphacite–orthopyroxene granulite is inferred to be a large inclusion within the common monzodioritic omphacite–garnet granulite host (surrounding the sketched outcrop). The single layer of omphacitic clinopyroxenite is interpreted to be a primary cumulate layer. In this outcrop, the large inclusion is inferred to have been injected by the protolith to the omphacite–garnet granulite forming reaction zones adjacent to the semi-continuous dykes. Labelled garnet-bearing veins involve euhedral garnet in leucocratic a plagioclase-rich matrix (see Clarke et al., 2013). Letters in squares denote sample sites referred to in other figure captions and text. b) Omphacite–orthopyroxene granulite component of the Breaksea Orthogneiss, comprising orthopyroxene in clusters surrounded by omphacite, in a feldspar-rich matrix, sample 1204A. c) Omphacite–orthopyroxene granulite (on the right) with a diffuse reaction zone, containing Type 2 garnet pseudomorphing ferromagnesian clusters in contact with an omphacite–garnet granulite dyke, sample 1204B. d) Pure omphacite layers with coronae of Type 2 garnet in reaction zones, adjacent to omphacite–orthopyroxene granulite, sample 1204D.

omphacite–garnet granulite in Breaksea Sound (Fig. 3d of De Paoli et al., 2009).

Omphacite–garnet granulite has local (cm-scale) variations in garnet and clinopyroxene mode alternating with feldspar forming a primary layering now transposed into an S_1 gneissic fabric. Centimetre-scale elongate clusters of granoblastic omphacite (14%), garnet (20%) and rutile (6%) are enclosed in a matrix dominated by plagioclase (40%), quartz (8%), K-feldspar (some as antiperthite: 7%) and kyanite (5%). Though mostly concentrated in clusters, omphacite and garnet also occur distributed throughout the plagioclase-rich matrix, elongate clusters and alignment of all minerals defining S_1. In rare cm-scale clusters, and in garnet strain-shadows, euhedral omphacite and feldspar occur intergrown with garnet (Fig. 3a). Large Type 1 garnet grains commonly have fine rutile exsolution through much of the inner grain core, and may have overgrowths of garnet and quartz mimicking the style of Type 2 garnet (Fig. 3b). Type 1 garnet may also have rare magnetite inclusions restricted to grain cores with rutile inclusions and exsolution in outer parts of the grains. Fine-grained symplectites of post-S_1 diopside and plagioclase partially pseudomorph omphacite (Fig. 3a).

The cores of *omphacite–orthopyroxene granulite* pods and layers comprise granoblastic plagioclase (46%), omphacite (18%), kyanite (11%), orthopyroxene (5–8%), quartz (6%), ulvöspinel (5%), and K-feldspar (some as antiperthite: 4%) with minor Type 1 garnet (~1%) and apatite (2%). Orthopyroxene and omphacite form cm-scale mafic clusters, large orthopyroxene grains (1–3 mm across) being mostly separated from the enclosing plagioclase-rich matrix by equigranular omphacite (Fig. 3c & d). Euhedral quartz (restricted to outer margins), plagioclase, omphacite, ulvöspinel and apatite inclusions occur randomly in orthopyroxene (Fig. 3c). Some grain cores of orthopyroxene and omphacite have acicular rutile exsolution needles, and, in places, blebs of exsolved ilmenite or pigeonitic pyroxene (Fig. 3d). Small (200–400 μm) omphacite grains define symmetrical to asymmetrical tails to clusters whereas large (1000 μm across) polygonal grains occur adjacent to orthopyroxene. Elongate ulvöspinel (500 μm), with fine exsolution lamellae of titano-ilmenite, occurs as the tails to attenuated clusters intergrown with small omphacite and apatite (400 μm), and rarely in cluster interiors as equant grains (Fig. 3c). Rare Type 1 garnet is present intergrown with omphacite, or as small grains in the feldspar-rich matrix (Fig. 3e). The grains are inclusion-free but may have rutile exsolution lamellae.

A polygonal mosaic of quartz, plagioclase, K-feldspar and kyanite with minor elongate flaser omphacite, apatite and ulvöspinel separates the mafic clusters. In places, large porphyroclastic feldspar grains are deformed and surrounded by a mantle of smaller grains, though most regions are granoblastic. Large tabulate to acicular (200–500 μm) kyanite (7%) is intergrown with plagioclase, quartz and K-feldspar, occurring in places as radiating splays or aligned in S_1 (Fig. 3e). Kyanite is partially pseudomorphed by coronae of plagioclase and/or fine-grained symplectites of plagioclase and magnetite (Fig. 5e). Clinozoisite is present along plagioclase grain boundaries as fine-grained rods that cut S_1. Thin symplectites of sodic diopside and albitic plagioclase commonly separate omphacite from plagioclase, quartz and K-feldspar.

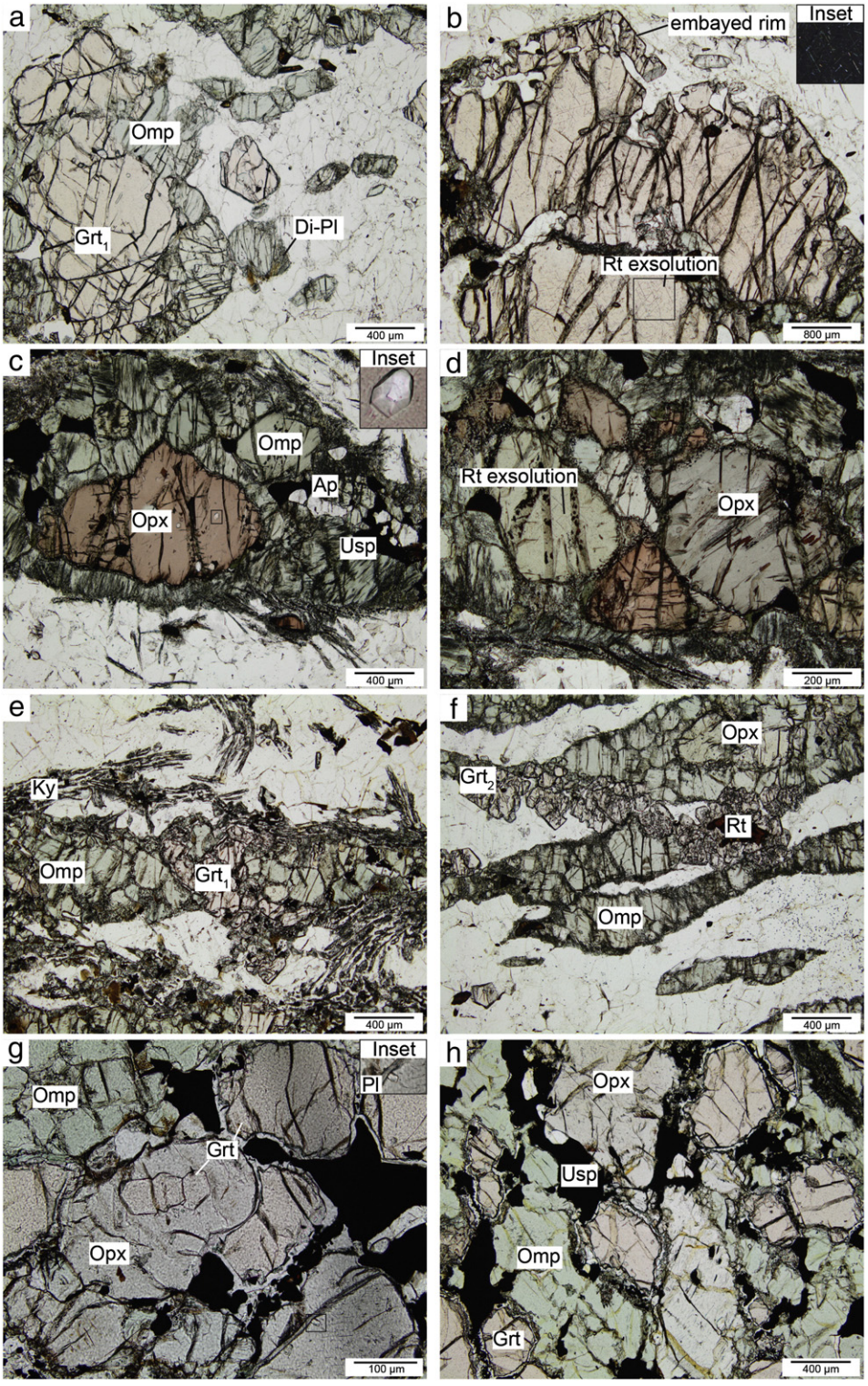

Fig. 3. a) Euhedral, weakly aligned omphacite intergrown with plagioclase in the strain shadow of Type 1 garnet, omphacite–garnet granulite sample 1206. b) Granoblastic Type 1 garnet in omphacite–garnet granulite with rutile exsolution-rich grain cores and embayed rim, mimicking Type 2 garnet. Inset is a cross polarised view of the rutile exsolution lamellae in the garnet core. Omphacite–garnet granulite sample 1204C. c) Orthopyroxene, omphacite and ulvöspinel within grain clusters surrounded by plagioclase and kyanite in omphacite–orthopyroxene granulite. Orthopyroxene is commonly armoured by omphacite. In tails a smaller omphacite is intergrown with ulvöspinel and apatite. Inset shows quartz inclusion (35 μm) in orthopyroxene exhibiting crystal faces. Sample 1204B-3. d) Adjacent orthopyroxene grains in the interior of a grain cluster; note apparent dihedral angles at coincident triple junctions. e) Rare Type 1 garnet intergrown with omphacite in omphacite–orthopyroxene granulite. Matrix includes splays of kyanite. Sample 1204H. f) Type 2 garnet formed at the contact of plagioclase and ferromagnesian clusters of omphacite and orthopyroxene in reaction zones. Omphacite clusters have high aspect ratios and flaser structures. Sample 1204B-1. g) Garnet and euhedral plagioclase inclusions (inset) within poikilitic orthopyroxene in clusters with a large garnet surrounded by ulvöspinel selvages and a matrix of omphacite. Fine plagioclase coronae mantle garnet, orthopyroxene eclogite, sample 0611B. h) Orthopyroxene and ulvöspinel, surrounded by omphacite and garnet in orthopyroxene eclogite. Sample 0611B.

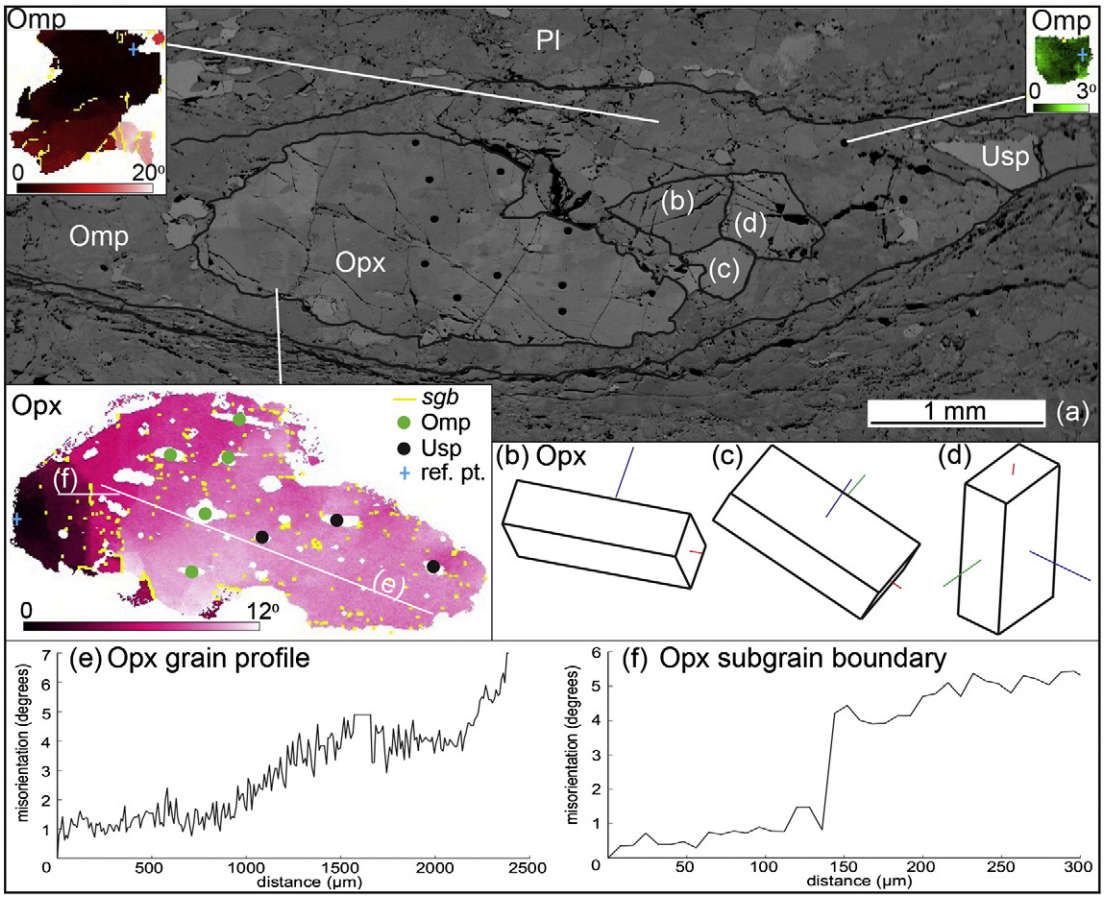

Fig. 4. Orientation contrast image of pyroxene grain cluster (sample 0905C) with crystallographic misorientation defined from a specified reference point (blue cross) for orthopyroxene (pink, inclusions labelled), large omphacite (red) and small recrystallised omphacite (green); low angle (2–10°) subgrain boundaries (*sgb*) are shown in yellow (a). Adjacent orthopyroxene crystals (b, c, d) have corresponding orthorhombic 3D crystallographic orientation diagrams, showing coincident facets to grain boundaries. Misorientation profile showing gradual lattice distortion (e) and subgrain boundary profile (f) in large orthopyroxene (pink).

Minor fine-grained symplectites of hornblende, ilmenite, quartz and plagioclase may also enclose omphacite, orthopyroxene and ulvöspinel. Biotite can occur partially to completely pseudomorphing pyroxene in clusters (Fig. 3e).

Reaction zone assemblages and textures are similar to omphacite–orthopyroxene granulite although have lower modes of orthopyroxene (that show a progressive decrease towards omphacite–garnet granulite contacts), omphacite and kyanite, and contain abundant Type 2 garnet partially to completely pseudomorphing omphacite and orthopyroxene clusters (Fig. 3f). Type 2 garnet forms comparatively small (300–500 μm) poikiloblastic grains with inclusions of quartz, apatite, rutile, monazite and plagioclase, centred on pyroxene–plagioclase margins. Rounded quartz inclusions can occur elongated subparallel to garnet boundaries (Fig. 3f). Intergrown with garnet are quartz, rutile, K-feldspar and accessory magnetite.

Orthopyroxene eclogite contains orthopyroxene (14%) and garnet (23%) grains enveloped by a granoblastic S_1 foliation comprising omphacite (51%), ulvöspinel (8%), rutile (1%), apatite (2%) and rare plagioclase (<1%). Anhedral ulvöspinel has thin exsolution lamellae of titano-ilmenite. Garnet and orthopyroxene commonly form cm-scale clusters mantled by ulvöspinel-rich selvages (Fig. 3g–h). Orthopyroxene has inclusions of apatite, garnet and plagioclase (Fig. 3g) and may include lamellae of exsolved pigeonitic clinopyroxene. Garnet and omphacite have inclusions of apatite and ulvöspinel that do not define a foliation. Needles of exsolved rutile are common in garnet, orthopyroxene and omphacite. In places a fine film of K-feldspar, with or without hornblende, separates garnet, orthopyroxene and omphacite.

4. Electron backscatter diffraction (EBSD) analysis

To determine the nature of microstructure formation in relation to deformation kinematics, focused EBSD analysis was undertaken on the omphacite–orthopyroxene granulite. A detailed microstructural and crystallographic orientation investigation was performed using scanning electron microscopy (SEM) based EBSD on a Zeiss EVO MA15 SEM housed at the Australian Research Council (ARC) National Key Centre for the Geochemical Evolution and Metallogeny of Continents (GEMOC), Macquarie University, Sydney. Polished thick sections (*c.* 100 μm: cut parallel to lineation and perpendicular to foliation) were analysed at an accelerating voltage of 20–30 kV, a beam current of 8 nA and a working distance of ~10 mm. The electron backscatter diffraction patterns were automatically acquired and indexed using the AZtec HKL Channel 5 acquisition software. The EBSD patterns were collected in regular grids where the sampling step size was 8 μm. Post-processing data filtering was undertaken to remove erroneous non-indexed points in the Channel 5 software.

Detailed EBSD analysis was concentrated on pyroxene grain clusters analysed for mineral chemistry within the omphacite–orthopyroxene granulite, to establish any systematic links between chemistry and recrystallisation. Crystallographic orientations of pyroxene grains are depicted in forescatter orientation contrast images displaying qualitatively changes in orientation in grey scale (Prior et al., 1996). In addition, misorientation maps, exhibiting the change in crystallographic orientation relative to a reference point (marked with blue cross) are utilised (Fig. 4a). 3D representation of crystal orientation is also provided

(Fig. 4b–d). Additional grain cluster orientation data is displayed in the supplementary material (Fig. S1). In the following analysis grains are defined as areas fully surrounded by grain boundaries with misorientations of greater than 10°; boundaries with misorientations between 2° and 10° are referred to as subgrain boundaries (*sgb*).

EBSD analysis shows that there are clusters of large to medium grained orthopyroxene grains directly associated with omphacite (Fig. 4a). Orthopyroxene is seen both with up to 30 μm omphacite inclusions or intergrown with coarse omphacite (400–600 μm). In addition, small grains of omphacite (150–400 μm) are seen surrounding these orthopyroxene–omphacite clusters. Grain boundaries between omphacite grains typically show equilibrium textures with near 120° triple junctions, whereas for orthopyroxene the apparent dihedral angles can be less than 120° (Fig. 3d). Within clusters, boundary traces of orthopyroxene are consistent with a low index plane, *i.e.* crystal facets (Fig. 4b–d). The crystal lattice of individual orthopyroxene grains is bent, showing both a gentle change in misorientation and distinct subgrain boundaries (Fig. 4e–f). Omphacite porphyroclasts adjacent to orthopyroxene show significant lattice distortion (5–20°) and subgrain boundary development, whereas smaller grains in tails are relatively free of substructure (3–4° of misorientation: Fig. 4a).

5. Whole-rock geochemistry

In addition to major element geochemistry previously analysed (Fig. 1b and Table 1) by De Paoli et al. (2009) and Clarke et al. (2013), REE contents were determined for omphacite–orthopyroxene granulite and omphacite–garnet granulite utilising whole-rock solutions analysed on an Agilent 7700cs Inductively Coupled Plasma Mass Spectrometer (ICPMS) at GEMOC, Macquarie University, Sydney (Table 1). Values were normalised to chondrite after Taylor and McLennan (1985). Omphacite–garnet and omphacite–orthopyroxene granulite, have nearly identical REE concentrations defined by slightly HREE depleted and Eu neutral to weakly positive signatures (Table 1).

Table 1
Whole-rock major element XRF (after Clarke et al., 2013; De Paoli et al., 2009) and REE (ppm) ICPMS solution analysis of components of the Breaksea Orthogneiss.

Sample lithology	1008B Omp–Grt granulite	1009B Omp–Opx granulite	0904C Eclogite	0611C Opx eclogite
SiO_2	54.05	53.56	42.18	47.52
TiO_2	1.06	1.01	1.88	2.09
Al_2O_3	18.34	18.23	16.97	10.51
Fe_2O_3	8.02	8.20	15.42	16.65
MnO	0.11	0.12	0.31	0.22
MgO	4.51	4.51	8.44	11.49
CaO	7.65	7.58	12.39	9.07
Na_2O	4.57	4.74	1.89	1.51
K_2O	1.30	1.31	0.02	0.28
P_2O_5	0.38	0.39	0.42	0.61
LOI	0.00	0.09	−0.25	0.29
Total	99.98	99.74	99.67	100.25
La	18.01	18.73	5.33	–
Ce	34.52	35.77	15.92	–
Pr	4.37	4.51	2.62	–
Nd	20.96	21.61	14.31	–
Sm	4.33	3.89	4.87	–
Eu	1.545	1.612	1.90	–
Gd	3.19	3.33	6.34	–
Dy	2.82	2.78	6.60	–
Ho	0.476	0.51	1.47	–
Er	1.36	1.266	4.24	–
Yb	1.162	1.377	4.06	–
Lu	0.167	0.189	0.63	–

LOI, loss on ignition.

6. Mineral chemistry

6.1. Analytical methods

The major element composition of rock-forming minerals was determined using polished thin sections and a CAMEBAX SX100 electron microprobe (EMP) housed at GEMOC, Macquarie University, Sydney. Operating conditions for the EMP involved 15 kV accelerating voltage and a beam current of 20 nA. Precision was typically less than 0.2 wt.% for the major elements based on 1σ distribution, consistent with GEMOC laboratory compilations (*e.g.* Norman et al., 1998). The trace element (including REE) composition of rock-forming minerals was determined through the *in-situ* analysis of grains in polished thick (*c.* 100 μm) sections using an Agilent 7700cs quadrupole ICPMS, attached to a New Wave 213 nm Nd:YAG laser ablation microprobe (LAM) housed at GEMOC, Macquarie University, Sydney. LA–ICPMS operating conditions and data acquisition parameters involved a *c.* 60 s background period count prior to laser ablation, and a *c.* 100–120 s analysis using a 55 μm beam diameter and 5 Hz pulse repetition rate. The laser beam power of 85–90% created flat bottom pits of *c.* 40 μm depth. The chondrite normalisation of reduced trace element data was made using values of Taylor and McLennan (1985) within the GLITTER software (http://www.glitter-gemoc.com). The analysis of NIST 610 glass during each session provided an external standard. Standard reference material BCR2, was analysed as an internal standard. Individual analyses were required to fall within error of long-term laboratory compilations (Norman et al., 1998). Precision was 1–8% relative standard deviation, based on 1σ distribution on all of the REE. Representative mineral chemistry datasets are presented in Table 2.

6.2. Major elements

The major element mineral chemistry for samples of the Breaksea Orthogneiss from Breaksea Sound and Breaksea Tops have been described by De Paoli et al. (2009) and Clarke et al. (2013). Mineral chemistry is extended here to include omphacite–orthopyroxene granulite and orthopyroxene eclogite. Ferric iron and stoichiometric corrections were made following Droop (1987). Pyroxene stoichiometry, site occupancies and end-member calculations were made after Morimoto (1989). Clinopyroxene end-member proportions are as follows: jadeite, $Jd = (2Na / (2Na + Ca + Mg + Fe^{2+})) \cdot (Al_{M1} / (Al_{M1} + Fe^{3+}_{M1}))$, aegirine, $Ae = (2Na / (2Na + Ca + Mg + Fe^{2+})) \cdot (Fe^{3+}_{M1} / (Al_{M1} + Fe^{3+}_{M1}))$ and diopside, $Di/Quad = (Ca + Mg + Fe^{2+}) / (2Na + Ca + Mg + Fe^{2+})$. Orthopyroxene end-member proportions include: wollastonite, $Wo = Ca / (Fe^{tot} + Mn + Mg + Ca)$, enstatite, $En = Mg / (Fe^{tot} + Mn + Mg + Ca)$ and ferrosilite, $Fs = (Fe^{tot} + Mn) / (Fe^{tot} + Mn + Mg + Ca)$.

Orthopyroxene is enstatite-rich hypersthene with end-member proportions of $En_{67–72}Fs_{25–30}$. The hypersthene grains have high alumina contents of up to 0.3 cations per formula unit (p.f.u.: on the basis of 6 oxygen) and appreciable Mg-Tschermak's component (MgTs: Fig. S2). Grains lack distinctive end-member zoning, though core to rim variation in Al of 0.3–0.1 p.f.u. is observed unrelated to subgrain boundaries. Most orthopyroxene in eclogite has compositions almost identical to hypersthene in granulite, lying in the range $Di_{0–1}En_{69–73}Fs_{27–30}$, with similar but less pronounced zoning in MgTs component (Fig. S2).

Clinopyroxene in omphacite–orthopyroxene granulite is omphacite (after Morimoto, 1989: Fig. 5). Jadeite content of $Jd_{20–28}$ is comparable to clinopyroxene in omphacite–garnet granulite ($Jd_{18–30}$) and eclogite ($Jd_{20–30}$), although aegirine content is slightly higher ($Ae_{9–13}$ *cf.* $Ae_{7–9}$ in omphacite–garnet granulite) highlighting higher ferric iron content (Fig. 6a). Grains in asymmetrical tails typically have higher jadeite proportions ($Jd_{20–26}$) than large grains in cluster centres ($Jd_{18–23}$), and are

Table 2
Representative mineral wt.% oxide, cations for a stated number of oxygen and REE (ppm) concentrations from electron microprobe and LA–ICPMS analysis.

	Omphacite–orthopyroxene granulite							
	0905C							
	Opx (core)	Opx (rim)	Omp (core)	Omp (rim)	Grt (Type 1)	Pl	Usp	Ilm
SiO_2	48.81	51.29	49.00	51.67	38.87	58.54	0.04	0.02
TiO_2	0.05	0.03	0.74	0.54	0.05	0.00	33.16	41.90
Al_2O_3	7.55	4.57	11.44	10.75	22	24.20	0.01	0.00
Cr_2O_3	0.02	0.00	0.01	0.01	0	0.00	0.05	0.05
FeO	18.73	19.01	9.01	7.97	23.43	0.40	62.83	54.45
MnO	0.77	0.89	0.22	0.33	1.17	0.00	0.20	0.25
MgO	23.86	24.40	8.27	10.37	10.29	0.05	0.51	0.66
CaO	0.13	0.22	16.76	14.61	5.23	7.36	0.01	0.00
Na_2O	0.14	0.03	4.11	4.39	0.07	7.01	0.01	0.01
K_2O	0.01	0.00	0.01	0.01	0	0.30	0.00	0.00
Total no.	100.07	100.43	99.56	100.64	101.11	97.86	96.83	97.34
O	6.00	6.00	6.00	6.00	12.00	8.00	3.00	4.00
Si	1.79	1.88	1.82	1.87	2.95	2.68	0.00	0.00
Ti	0.00	0.00	0.02	0.01	0.00	0.00	0.95	0.80
Al	0.33	0.20	0.50	0.46	1.97	1.30	0.00	0.00
Cr	0.00	0.00	0.00	0.00	0.00	0.00	0.00	0.00
Fe	0.58	0.58	0.28	0.24	1.49	0.02	2.01	0.40
Mn	0.02	0.03	0.01	0.01	0.08	0.00	0.01	1.77
Mg	1.31	1.33	0.46	0.56	1.16	0.00	0.03	0.00
Ca	0.00	0.01	0.67	0.57	0.42	0.36	0.00	0.03
Na	0.01	0.00	0.30	0.31	0.01	0.62	0.00	0.00
K	0.00	0.00	0.00	0.00	0.00	0.02	0.00	0.00
Total	4.05	4.02	4.05	4.04	8.07	5.00	3.00	3.00
La	0.61	0.26	4.40	3.79	0.34	–	0.03	–
Ce	1.50	1.41	21.33	19.45	0.33	–	0.07	–
Pr	0.13	0.31	4.56	4.15	0.19	–	0.01	–
Nd	0.55	1.63	25.68	22.33	2.01	–	0.04	–
Sm	0.07	0.54	7.31	6.88	2.95	–	<LLD	–
Eu	0.04	0.20	2.41	2.30	1.81	–	<LLD	–
Gd	0.11	0.67	6.80	6.21	5.22	–	0.01	–
Dy	0.14	0.61	6.07	6.11	5.72	–	<LLD	–
Ho	0.04	0.13	1.18	1.18	1.26	–	<LLD	–
Er	0.05	0.45	3.45	3.08	4.24	–	0.01	–
Yb	0.06	0.51	3.15	3.17	6.25	–	0.02	–
Lu	0.01	0.10	0.42	0.42	1.15	–	<LLD	–

	Reaction zone							
	1009A							
	Opx (core)	Opx (rim)	Omp (core)	Omp (rim)	Grt 2 (core)	Grt 2 (rim)	Pl	Rt
SiO_2	50.83	52.93	48.80	49.32	38.82	38.55	61.37	0.19
TiO_2	0.07	0.05	0.79	0.78	0.05	0.06	0.01	97.25
Al_2O_3	5.51	1.48	11.01	11.53	22.26	21.88	23.39	0.00
Cr_2O_3	0.00	0.02	0.02	0.05	0.01	0.00	0.00	0.03
FeO	17.53	19.20	8.80	9.13	22.74	23.50	0.37	0.64
MnO	0.14	0.17	0.15	0.03	0.53	0.59	0.01	0.02
MgO	24.87	25.57	8.13	7.74	8.85	8.28	0.02	0.00
CaO	0.66	0.23	17.16	16.92	7.84	7.52	5.71	0.27
Na_2O	0.12	0.02	4.22	4.34	0.07	0.03	8.55	0.04
K_2O	0.02	0.01	0.02	0.02	0.01	0.02	0.18	0.00
Total no.	99.76	99.69	99.09	99.85	101.19	100.44	99.61	98.44
O	6.00	6.00	6.00	6.00	12.00	12.00	8.00	2.00
Si	1.86	1.95	1.83	1.83	2.94	2.94	2.73	0.00
Ti	0.00	0.00	0.02	0.02	0.00	0.00	0.00	0.99
Al	0.24	0.06	0.49	0.50	1.97	1.97	1.23	0.00
Cr	0.00	0.00	0.00	0.00	0.00	0.00	0.00	0.00
Fe	0.54	0.59	0.28	0.28	1.43	1.50	0.01	0.02
Mn	0.00	0.01	0.00	0.00	0.03	0.04	0.00	−0.01
Mg	1.35	1.40	0.45	0.43	0.98	0.94	0.00	0.00
Ca	0.03	0.01	0.69	0.67	0.66	0.61	0.27	0.00
Na	0.01	0.00	0.31	0.31	0.00	0.00	0.74	0.00
K	0.00	0.00	0.00	0.00	0.00	0.00	0.01	0.00
Total	4.03	4.02	4.06	4.05	8.00	8.00	5.00	1.00
La	0.74	0.49	8.06	3.35	0.62	0.19	–	0.08
Ce	1.89	0.96	24.35	16.34	1.87	0.62	–	0.48
Pr	0.21	0.13	4.36	3.61	0.36	0.17	–	0.04
Nd	0.93	0.36	23.49	21.34	2.64	2.47	–	0.72
Sm	0.22	0.05	6.86	6.20	4.25	4.56	–	0.12
Eu	0.04	0.02	2.44	1.72	2.32	2.68	–	0.06
Gd	0.14	0.05	6.41	3.86	9.05	9.36	–	0.07
Dy	0.08	0.16	6.17	2.14	8.34	8.23	–	<LLD
Ho	0.01	0.03	1.20	0.35	1.36	1.28	–	<LLD

Table 2 *(continued)*

	Reaction zone							
	1009A							
	Opx (core)	Opx (rim)	Omp (core)	Omp (rim)	Grt 2 (core)	Grt 2 (rim)	Pl	Rt
Er	<LLD	0.09	3.06	0.80	3.20	2.89	–	0.09
Yb	0.02	0.06	2.68	0.48	2.72	1.80	–	0.11
Lu	<LLD	0.01	0.36	0.08	0.30	0.22	–	<LLD

	Orthopyroxene eclogite						
	0611B						
	Opx (core)	Opx (rim)	Omp (core)	Omp (rim)	Grt (core)	Grt (rim)	Usp
SiO_2	55.43	54.10	53.44	53.56	38.79	39.18	0.05
TiO_2	0.05	0.01	0.26	0.18	0.10	0.12	38.70
Al_2O_3	2.58	1.42	5.80	5.48	21.70	21.72	0.08
Cr_2O_3	0.01	0.00	0.00	0.07	0.02	0.00	0.04
FeO	16.66	19.02	8.08	8.18	23.37	23.71	54.32
MnO	0.17	0.19	0.09	0.07	0.71	0.85	0.09
MgO	25.76	25.90	10.80	10.93	10.59	10.61	2.03
CaO	0.86	0.20	17.19	17.36	4.55	4.43	0.14
Na_2O	0.16	0.02	3.81	3.83	0.02	0.01	0.01
K_2O	0.13	0.00	0.01	0.01	0.01	0.00	0.00
Total no.	101.81	100.87	99.48	99.69	99.86	100.62	95.45
O	6.00	6.00	6.00	6.00	12.00	12.00	3.00
Si	1.97	1.96	1.97	1.98	2.97	2.97	0.00
Ti	0.00	0.00	0.01	0.01	0.01	0.01	0.81
Al	0.11	0.06	0.25	0.24	1.96	1.94	0.00
Cr	0.00	0.00	0.00	0.00	0.00	0.00	0.00
Fe	0.49	0.58	0.25	0.25	1.49	1.51	1.27
Mn	0.01	0.01	0.00	0.00	0.05	0.05	0.00
Mg	1.36	1.40	0.59	0.60	1.21	1.20	0.08
Ca	0.03	0.01	0.68	0.69	0.37	0.36	0.00
Na	0.01	0.00	0.27	0.27	0.00	0.00	0.00
K	0.01	0.00	0.00	0.00	0.00	0.00	0.00
Total	3.99	4.01	4.03	4.04	8.05	8.05	2.18
La	0.32	0.28	7.65	3.69	0.14	<LLD	0.26
Ce	1.32	1.14	20.29	18.87	0.41	0.05	0.83
Pr	0.29	0.24	3.62	4.24	0.06	0.04	0.14
Nd	1.60	1.31	20.69	24.91	0.35	1.05	0.66
Sm	0.51	0.35	6.33	7.46	0.08	2.23	0.17
Eu	0.11	0.07	1.26	1.54	0.02	0.86	0.03
Gd	0.42	0.35	4.80	5.49	0.10	6.34	0.16
Dy	0.17	0.17	2.10	2.45	0.06	12.44	0.09
Ho	0.03	0.02	0.21	0.29	0.02	2.90	0.01
Er	0.03	0.05	0.24	0.39	0.02	8.60	0.03
Yb	0.03	<LLD	0.07	0.16	0.04	8.76	<LLD
Lu	0.01	0.01	0.00	0.02	0.00	1.26	<LLD

similar to contents in reaction zones (Jd_{23-25}). There is also a continuous rimward zoning to Na-diopside-rich rims ($Jd_{20-25}Ae_{5-12}Q_{68-75}$) from jadeite-enriched cores ($Jd_{25-28}Ae_{9-13}Q_{63-66}$). Clinopyroxene in the orthopyroxene eclogite components is omphacite with grain cores of $Jd_{17-22}Ae_{2-7}Q_{71-76}$ and grain rims of $Jd_{15-18}Ae_{7-10}Q_{73-75}$. The dominant exchange trends evident in clinopyroxene can be observed on a J = 2Na *versus* Q = (Ca + Mg + Fe^{2+}) diagram (after Morimoto, 1989), with chemical variation defining a linear trend between jadeite and diopside/hedenbergite, more or less at fixed to slightly decreasing Ca-Tschermak's component (CaTs: Fig. 5). Omphacite in orthopyroxene eclogite has lower CaTs- and Jd-component compared to granulite components, but similar within-sample core to rim variability.

Garnet end-member proportions were determined using the following calculations: pyrope, Prp = Mg / (Fe^{2+} + Mn + Mg + Ca), almandine, Alm = Fe^{2+} / (Fe^{2+} + Mn + Mg + Ca), grossular, Grs = (Ca / (Fe^{2+} + Mn + Mg + Ca)) − (And + Uv), spessartine, Sps = Mn / (Fe^{2+} + Mn + Mg + Ca), andradite, And = Fe^{3+} / (Fe^{3+} + Al^{VI} + Cr + Ti) and uvarorite, Uv = Cr / (Fe^{3+} + Al^{VI} + Cr + Ti), with Al^{VI} = Al − (3-Si). Rare garnet in omphacite–orthopyroxene granulite has contents of $Alm_{41-45}Prp_{31-39}Grs_{6-12}Sps_{1-2}And_{8-10}$ that are largely comparable to Type 1 garnet in omphacite–garnet granulite, except for higher andradite contents (*cf.* $Alm_{41-43}Prp_{39-41}Grs_{8-10}Sps_1And_{6-8}$: Fig. 6b). Rims are marginally more enriched in grossular (Grs_{10-15}) with lower pyrope contents (Prp_{34}). In reaction zones, garnet cores of $Alm_{42-44}Prp_{28-30}Grs_{17-19}Sps_{0-1}And_{7-8}Uv_{0-0.1}$ are enclosed by rims of $Alm_{42-47}Prp_{30-34}Grs_{16-17}Sps_{0-1}And_{8-10}Uv_{0-0.1}$ (*cf.* Type 2 garnet from omphacite–garnet granulite: $Alm_{40-45}Prp_{32-37}Grs_{14-20}Sps_1And_{3-6}$). Garnet in orthopyroxene eclogite has lower Grs contents and slightly higher Prp contents compared to both Type 1 & 2 garnets in granulite ($Alm_{45-52}Prp_{39-42}Grs_{2-10}Sps_{1-2}And_{5-8}Uv_{0-0.1}$).

Feldspar end-member proportions were calculated as follows: Anorthite, An = Ca / (Ca + Na + K), Albite, Ab = Na / (Ca + Na + K) and Orthoclase, Or = K / (Ca + Na + K). Feldspar in omphacite–orthopyroxene granulite occurs as plagioclase and K-feldspar. Plagioclase is oligoclase to andesine in composition ($An_{18-35}Ab_{65-82}Or_{0-10}$), with symplectite plagioclase richer in anorthite (An_{35-50}). The matrix plagioclase compositions are comparable to that in the omphacite–garnet granulite ($An_{11-36}Ab_{63-87}Or_{1-2}$: De Paoli et al., 2009). K-feldspar is microcline with compositions of $An_{0-5}Ab_{0-15}Or_{82-90}$.

Accessory oxide phases were also characterised using stoichiometry and cation distribution. Oxide in the omphacite–orthopyroxene granulite and orthopyroxene eclogite is mostly ulvöspinel. Exsolution lamellae in hosts of ulvöspinel have higher TiO_2 content and reflect a

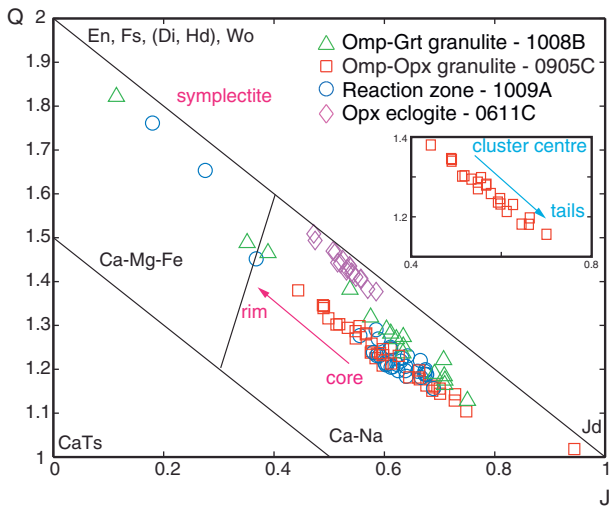

Fig. 5. Binary plot with axes Q = Ca + Mg + Fe^{2+} and J = 2Na after Morimoto (1989) of clinopyroxene microprobe analysis from some components of the Breaksea Orthogneiss. Inset shows linear increase in jadeite content from relict grains to recrystallised grains in cluster tails.

separate titano-ilmenite phase. In both granulite and eclogite the ulvöspinel host has Fe^{3+} of 1.1–1.2 p.f.u. (on the basis of 4 oxygen) and Fe^{2+} of 1.37–1.52 p.f.u. compared to the titano-ilmenite exsolution lamellae with $Fe^{3+} \approx 0.3$–0.4 p.f.u. (on the basis of 3 oxygen) and

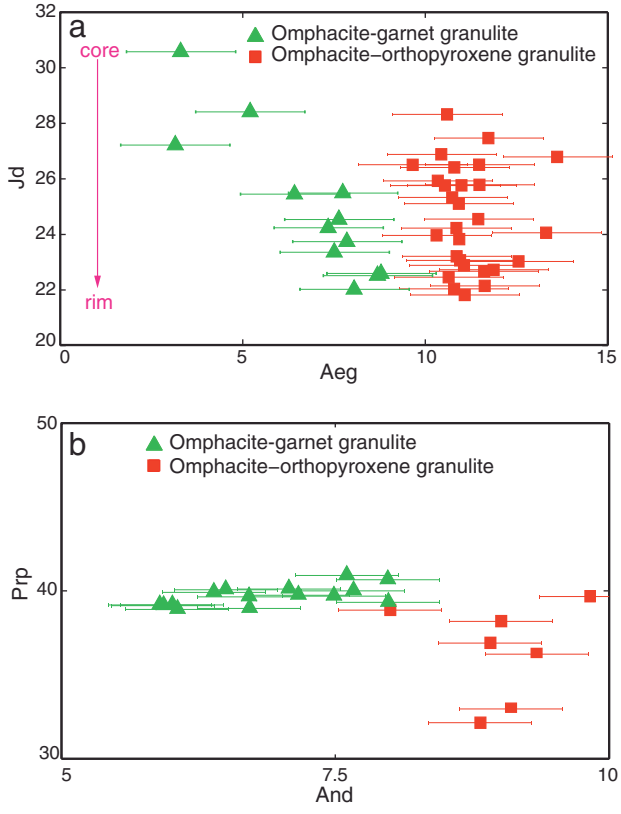

Fig. 6. (a) Clinopyroxene Aeg [=2Na / (2Na + Ca + Mg + Fe^{2+}) · Fe^{3+}_{M1} / (Al_{M1} + Fe^{3+}_{M1})] *vs.* Jd [=2Na / (2Na + Ca + Mg + Fe^{2+}) · (Al_{M1} / (Al_{M1} + Fe^{3+}_{M1}))] and (b) garnet And [=Fe^{3+} / (Fe^{3+} + Al^{VI} + Cr + Ti)] *vs.* Prp [=Mg / (Fe^{2+} + Mn + Mg + Ca)] binary plots, emphasizing variation in iron (ferric) between omphacite–garnet granulite and omphacite–orthopyroxene granulite components. Stoichiometry and ferric iron correction after Droop (1987) and Morimoto (1989). Uncertainty based on conservative Fe analytical error (0.2 wt.%); error is within symbols in the *y*-dimension.

$Fe^{2+} \approx 0.75$ p.f.u. Symplectite ilmenite intergrown with plagioclase on orthopyroxene has $Fe^{3+} \approx 0.82$ p.f.u.

6.3. Trace elements

Trace element mineral compositions have been described for Breaksea Orthogneiss samples from Breaksea Tops by Clarke et al. (2013), and additional mineral chemistry is provided here to include omphacite–orthopyroxene granulite and orthopyroxene eclogite.

Chondrite-normalised REE data for clinopyroxene in omphacite–orthopyroxene granulite define a concave-down bell-shaped pattern between La and Dy with an inflection at Nd. Omphacite in these rocks differs from other components of the Breaksea Orthogneiss in having higher total REE content (10–25 times compared to 3–15 times chondrite: Fig. 7a–b). In addition, light-REE (LREE) content is slightly more enriched and the bell-shaped peak centred on the middle-REE (MREE) is more pronounced. The largest within-sample variation occurs with a prominent enrichment of the heavy-REE (HREE) content (5–15 times compared to 3 times chondrite). Core to rim zoning in REE content of clinopyroxene in reaction zones involves decreasing REE content (Fig. 7c–d). Rims are depleted in HREE compared to grain cores, with values similar to those of omphacite in omphacite–garnet granulite. Clinopyroxene in orthopyroxene eclogite has REE patterns similar to those in omphacite–orthopyroxene granulite, although is depleted in MREE–HREE and contains a pronounced negative Eu anomaly, overall with a lower total REE content (Fig. 7e–f).

Orthopyroxene REE content varies with mineral association, but overall shows depleted concave-up patterns in granulite components. In omphacite–orthopyroxene granulite the pattern involves subtle HREE enriched contents with a peak at values of 1–1.5 times chondrite, and flat-lying MREE trend with declining LREE (Fig. 8a). REE content in subgrains maintain similar patterns and concentrations, lying within the analysed within-sample range of both cores and rims (Fig. 8a & Table S1). Reaction zone orthopyroxene shows a comparative depletion in the HREE, with minor enrichment in LREE (1–4.5 times chondrite: Fig. 8b). Rims have slightly more HREE content than cores (4–10 times chondrite). Orthopyroxene in eclogite show similar depleted trends to orthopyroxene in granulite, being most pronounced with LREE depletion (Fig. 8c).

Rare igneous Type 1 garnet in omphacite–orthopyroxene granulite exhibits an exponential increase in REE content from LREE to MREE, with a general trend of increasing HREE content above an inflection point at Eu (Fig. 9a–b). The trend involves a subtle flat, to positive Eu anomaly. Rims are characterised by lower HREE contents and Eu positive trends, mimicking patterns of Type 2 garnet (Fig. 9a & b). The HREE-enriched core pattern overlaps with igneous Type 1 garnet in omphacite–garnet granulite and eclogite (Clarke et al., 2013), though is typically slightly more HREE-enriched. REE patterns for garnet in reaction zones define a concave-down chevron shape characteristic of metamorphic Type 2 garnet (Clarke et al., 2013). The pattern is strongly depleted in the LREE, with a steep peak in the MREE from Nd to Eu, the Eu anomaly providing a trend inflection point (Fig. 9c–d). The HREE content is slightly enriched with values of 3–15 times chondrite, but HREE content decreases with increasing atomic mass. Garnet in orthopyroxene eclogite defines a gently curved concave-down pattern, with an inflection point in the upper MREE, depletion in Eu and pronounced HREE enrichment, that is slightly greater than garnet from eclogite (Fig. 9e–f: Clarke et al., 2013).

Ulvöspinel, ilmenite and rutile have a uniformly depleted REE content, with values close to, or below, the lower limits of detection (LLD: Table S1). In contrast, apatite maintains LREE-enriched and HREE-depleted patterns throughout components of the orthogneiss (see Clarke et al., 2013).

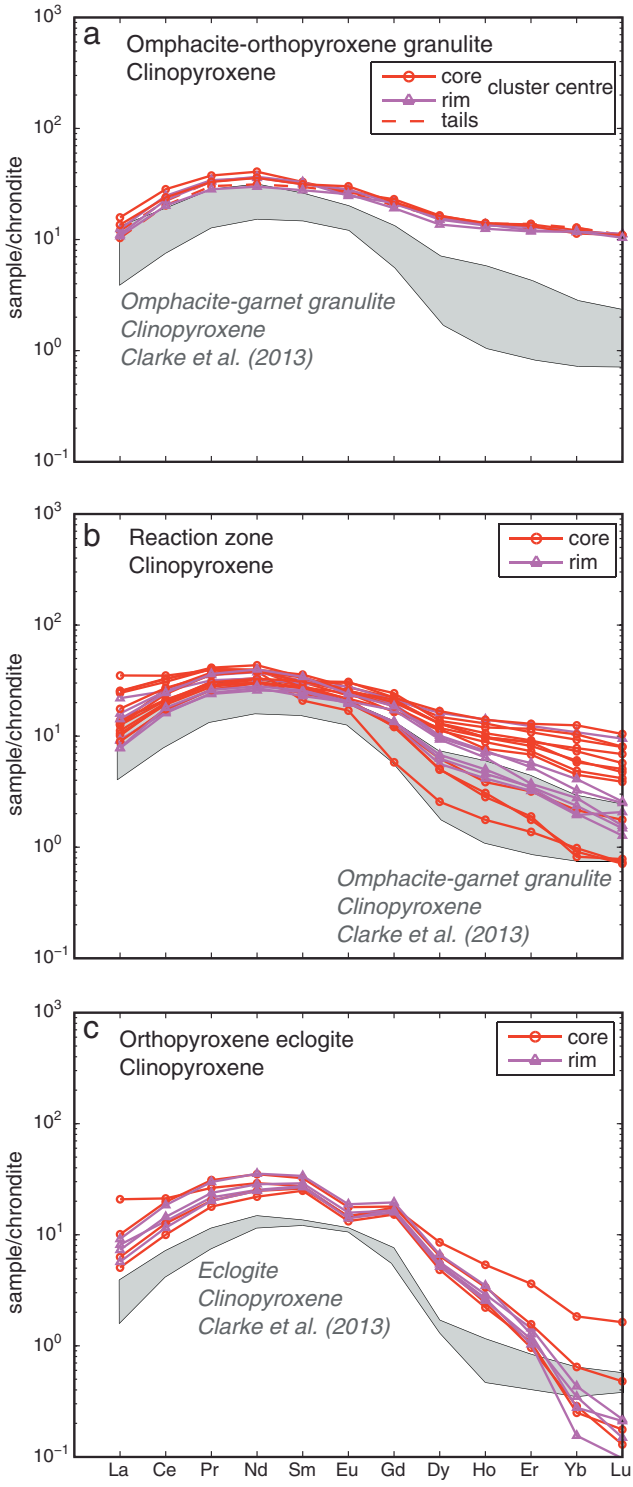

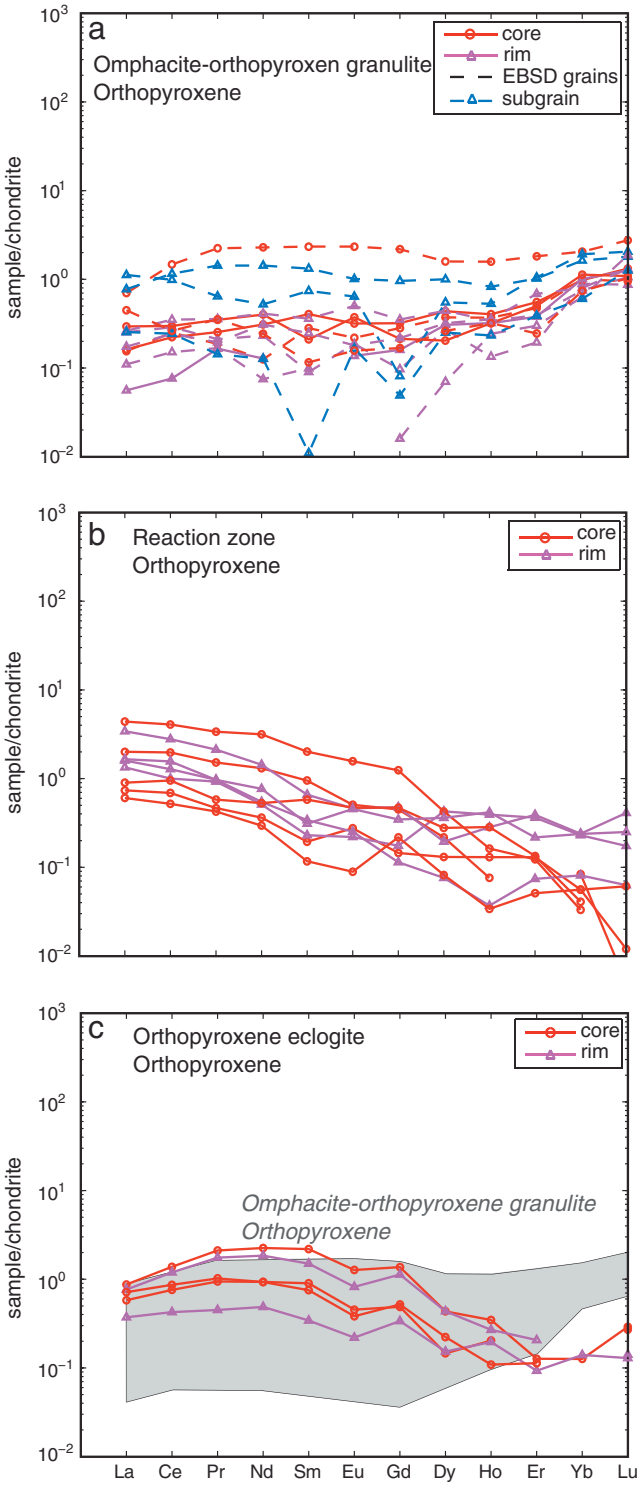

Fig. 7. Chondrite-normalised REE (after Taylor and McLennan, 1985) data for clinopyroxene in: (a) omphacite–orthopyroxene granulite, (c) reaction zones and (e) orthopyroxene eclogite. Grey shading represents the range of REE compositions for clinopyroxene from components of Breaksea Orthogneiss from Clarke et al. (2013). Note HREE enrichment of omphacite in omphacite–orthopyroxene granulite compared to omphacite from omphacite–garnet granulite and progressive HREE depletion with proximity to Type 2 garnet in reaction textures (rims).

Fig. 8. Chondrite-normalised (after Taylor and McLennan, 1985) REE data for orthopyroxene in omphacite–orthopyroxene granulite (dashed lines represent grains analysed by EBSD): (a) reaction zones (b) and orthopyroxene eclogite. (c) Grey shading provided for comparison between orthopyroxene REE compositions. Contents across subgrains are distributed within the sample spread. Orthopyroxene in reactions zones and orthopyroxene eclogite are subtly more depleted in HREE content.

7. Discussion

The formation of orthopyroxene, omphacite, plagioclase, ulvöspinel and garnet within omphacite–orthopyroxene granulite and orthopyroxene-eclogite begs an explanation in the wider context of petrogenetic histories interpreted for the Breaksea Orthogneiss (*e.g.* Clarke et al., 2013; De Paoli et al., 2009, 2012). Mineral equilibria modelling by De Paoli et al. (2012) posits an 0.8 GPa pressure difference between the upper limit of orthopyroxene stability in the granulite facies (for a monzodioritic protolith) and peak conditions inferred for

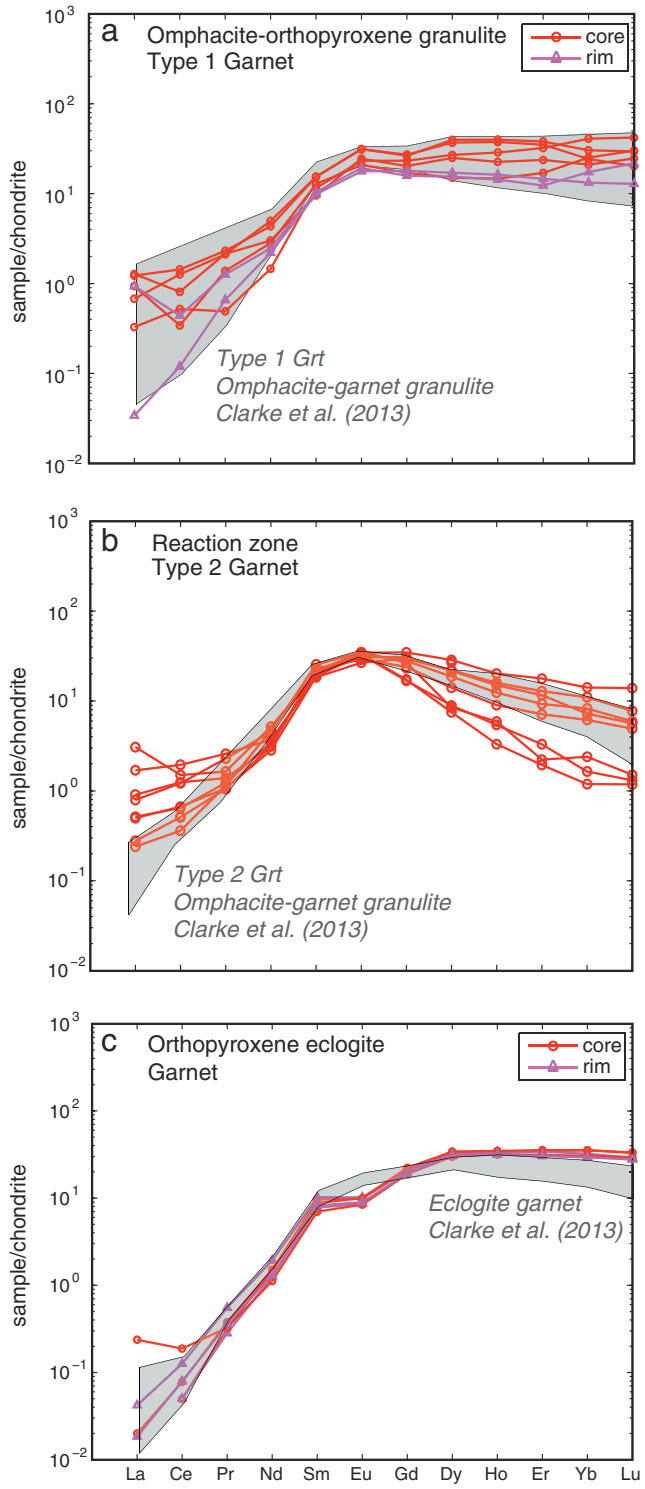

Fig. 9. Chondrite-normalised (after Taylor and McLennan, 1985) REE data for (a) Type 1 garnet in omphacite–orthopyroxene granulite, (c) Type 2 garnet in reaction zones, and (e) garnet in orthopyroxene eclogite. Grey shading represents the range of REE compositions for garnet types from other components of the Breaksea Orthogneiss after Clarke et al. (2013). Note the overlap of the Type 1 garnet core trends to that of omphacite–garnet granulite and progressive HREE zoning that mimic Type 2 garnet depleted contents. Orthopyroxene eclogite trends vary significantly from the common eclogite trends in HREE and Eu contents.

the Breaksea Orthogneiss ($P \approx 1.8$ GPa and $T \approx 850$ °C; omphacite granulite and eclogite facies). A subtle reduction in the P difference to 0.6–0.7 GPa is predicted by modelling at more oxidising conditions, a consequence of reaction suppression by the ferric-rich orthopyroxene (De Paoli et al., 2012). The high alumina contents and presence of pigeonitic exsolution in orthopyroxene are consistent with high-T (>1000 °C: Bohlen and Essene, 1978; Harley, 1984; Sandiford and Powell, 1986) and high-P conditions (*c.* 1.5–1.8 GPa: De Paoli et al., 2009). The absence of any solid-state reaction relationship between orthopyroxene and omphacite in the Breaksea Orthogneiss argues against a dynamic *PT* history to explain the observed assemblage, *via*, for example, the metastable persistence of orthopyroxene to high-P conditions following terrane burial.

Common mineral assemblages (including distinct Fe–Ti oxides), gradation in garnet–clinopyroxene–orthopyroxene–plagioclase modes between samples, and similarities in major and trace element compositions of key phases argues for a cogenetic igneous relationship between protoliths of orthopyroxene eclogite and omphacite–orthopyroxene granulite, similar to the cumulate relationships inferred for omphacite–garnet granulite, eclogite, garnetite and clinopyroxenite protoliths (Clarke et al., 2013). The 0.6–0.8 GPa pressure difference separating orthopyroxene- and omphacite-bearing granulite (De Paoli et al., 2012) makes a cogenetic metamorphic origin implausible. The igneous interpretation circumvents the paradox of metamorphic pyroxene stability but is reliant on the metastable persistence of igneous minerals in metamorphic rocks. The establishment of the extent of recrystallisation and metamorphism is required, particularly in the high variance assemblages of orthopyroxene-bearing granulite, to test the veracity of an igneous origin for the mineral assemblages.

7.1. Distinguishing igneous and metamorphic assemblages and microstructures

Omphacite–orthopyroxene granulite occurs as pods and discontinuous, centimetre- to decametre-layers in an omphacite–garnet granulite host, separated by diffuse garnet-bearing reaction zones. Whole-rock compositions of omphacite–orthopyroxene granulite and omphacite–garnet granulite are nearly identical (Fig. 1b and Table 1), yet the rocks have distinct mineral assemblages. Less silicic inclusions in the omphacite–garnet granulite include eclogite, and composite garnetite–clinopyroxenite bodies that include metre-scale layers formed almost entirely (>90%) of garnet or diopside (Clarke et al., 2013; De Paoli et al., 2009). The irregular distribution, range in silica content and scale of the inclusions make it highly unlikely that they could be formed through the metasomatic alteration of a once uniform omphacite–garnet granulite body (Clarke et al., 2013). Gross features of the Breaksea Orthogneiss can be interpreted in terms of cumulate processes, with igneous mineral chemistry persisting in much of the eclogite, garnetite and clinopyroxenite bodies (see Section 2.2 and Clarke et al., 2013).

Textures of omphacite–garnet granulite and omphacite–orthopyroxene granulite are nearly identical, though pluton-scale heterogeneity exists. Omphacite–garnet granulite includes decimetre-scale low-strain domains (enveloped by an S_1 gneissic foliation) characterised by randomly oriented or weakly aligned, euhedral garnet (Type 1), omphacite and plagioclase. These partially interlocking textures are arguably of igneous origin involving minimal grain shape changes (see also Vernon et al., 2012; Clarke et al., 2013) and provide a 'baseline' fabric to compare to microstructures as discussed in detail below. Igneous microstructures and chemistry have survived recrystallisation in such low-strain domains (*e.g.* Racek et al., 2008; Štípská and Powell, 2005; Vernon et al., 2012) or in minerals that are difficult to recrystallise, as highlighted by the preservation of igneous Type 1 garnet compositions in the omphacite–garnet granulite (Clarke et al., 2013). The rare Type 1 garnet in omphacite–orthopyroxene granulite is also considered igneous, based on similarities in REE content with garnet identified as igneous in eclogite and garnetite (Fig. 9a–b; Clarke et al., 2013). The igneous texture and growth stage in both instances is partially overprinted by a minor metamorphic re-equilibration rim (~30 μm; Fig. 3b) involving HREE and grossular zoning that mimics Type 2 garnet (lower HREE and higher Grs).

Outside these patchy low-strain domains of the Breaksea Orthogneiss, metamorphic textures involving Type 2 garnet and quartz intergrowths in reaction zones are well developed. The positive Eu anomaly, higher grossular content and distinct HREE-depleted pattern of Type 2 garnet are consistent with it being metamorphic, neoblasts having formed by a reaction between omphacite and plagioclase. Omphacite in these domains shows progressive HREE depletion in addition to subtly higher-jadeite and lower Ca-Tschermak's content grading towards garnet compared to homogenous clinopyroxene concentrations in omphacite–orthopyroxene granulite (Figs. 5 & 7c–d). This contrast suggests that omphacite has re-equilibrated with neocrystallised garnet and plagioclase, though element diffusion was limited to grains and/or margins adjacent to garnet. The depleted HREE content in Type 2 garnet is considered therefore a consequence of small diffusion distances and relative proximity to reactant elemental sinks (away from HREE-enriched Type 1 garnet, pyroxene and LREE-enriched apatite). The limited spatial extent of metamorphic reaction in these intergrown microstructures coupled with the patchy preservation of igneous garnet implies that a combination of igneous and metamorphic features are still present in the intermediately strained omphacite–orthopyroxene granulite.

Grain clusters in omphacite–orthopyroxene granulite comprise interiors of large equant (sometimes prismatic) orthopyroxene, omphacite and rare igneous Type 1 garnet, enveloped by smaller omphacite grains intergrown with elongated apatite and ulvöspinel (Figs. 3c & 4a). Orthopyroxene in cluster interiors can maintain apparent dihedral angles of less than 120° at some triple junctions (Fig. 3d) consistent with grain impingement during growth from a liquid (Vernon, 1970; Holness et al., 2012). Elsewhere grain shape changes to subsequently reduce interfacial energy, result in 120° orthopyroxene triple junctions (Fig. 4a: *e.g.* Holness et al., 2012). Yet, crystal facets of adjacent grains are preserved in a parallel orientation without significant rounding (Figs. 4b–d), and inclusions of quartz and plagioclase maintain euhedral faces in such grains (Fig. 3c & g). These features are consistent with the unimpeded magmatic growth of orthopyroxene, with variable but generally minimal textural equilibration during metamorphism (Holness et al., 2005; Vernon, 2014).

Establishing mineral growth stages relative to S_1 kinematics provides an additional test for inferences of mineral origins. At the grain-scale orthopyroxene is highly deformed with significant crystallographic misorientation (up to 12°) within one grain, mostly localised in low angle subgrain boundaries located close to the margin of grains. These features can be attributed to crystal-plastic deformation where some recovery aided the formation of distinct subgrain boundaries (Fig. 4). However, there are no new (smaller) grains observed surrounding porphyroclasts that would be consistent with recrystallisation during deformation, formed by either subgrain rotation or spontaneous nucleation (*e.g.* Svahnberg and Piazolo, 2010). The absence of chemical zoning of hypersthene, including MgTs content, across subgrains (Fig. 9a), is consistent with minimal intracrystalline diffusion having proceeded during, or related to S_1 crystal plastic deformation or substructure development (*cf.* Lund et al., 2006). As the high-alumina concentrations in orthopyroxene are incompatible with the *P–T* estimates of S_1 (1.8 GPa and 800–850 °C: De Paoli et al., 2009), this implies that most of the orthopyroxene chemistry originated from pre-S_1 conditions. Together with the preservation of plutonic textural relationships and disequilibrium metamorphic phase assemblages for the inferred peak conditions it is interpreted that orthopyroxene is a relict igneous phase, that lacked any high-*T* metamorphic overprint prior to S_1. Minor major element diffusion is likely to have occurred along grain rims during post-S_1 cooling and/or decompression, contemporary with the development of diopside–plagioclase and hornblende–plagioclase symplectite (Fig. S2; De Paoli et al., 2009).

In contrast to orthopyroxene, omphacite has not only deformed plastically during deformation resulting in intracrystal lattice bending, but also is recrystallised, producing new grains with limited substructure in cluster tails. These small grains surround large plastically deformed and elongated omphacite porphyroclasts (Figs. 3a–f & 4a). Subgrain rotation recrystallisation is considered responsible primarily for the development of new grains, on the basis of undulose extinction in omphacite and the similarity in subgrain sizes between porphyroclast and recrystallised grains (Svahnberg and Piazolo, 2010; Urai et al., 1986). However, grain boundaries may have readjusted by minor grain boundary migration. Recrystallisation went hand-in-hand with changes in the major element mineral composition, but not the REE content, of old and new omphacite grains (Figs. 5 & 7a–b). Porphyroclasts exhibit subtly lower jadeite contents ($Jd_{18–23}$) compared to grains in cluster tails ($Jd_{20–26}$). These microstructural relationships are consistent with the stability of porphyroclastic omphacite prior to solid-state recrystallisation, either from the igneous protolith or an enigmatic pre-S_1 metamorphism. In contrast, small jadeite-rich omphacite in flaser tails intergrown with elongated ulvöspinel and apatite form part of a substructure-free recrystallised, recovered (texturally mature grain boundaries) and partially equilibrated S_1 assemblage.

Textural and geochemical relationships in omphacite–orthopyroxene granulite, outside of reaction zones, are therefore consistent with most key minerals preserving compositions from the igneous protolith, particularly REEs, despite high-*T* (800–850 °C) and intermediate- to high-strain metamorphic conditions (Table 3). Similarly some accessory phases, such as ulvöspinel and LREE-enriched apatite are interpreted to have recrystallised with minor chemical change, as comparable grains occur adjacent to, or as inclusions within, igneous relicts. Relationships within reaction zones are consistent with the incomplete metamorphic equilibration of metastable igneous assemblages within localised domains (*cf.* Daczko and Halpin, 2009).

A progression from igneous textures, similar to those seen in undeformed or low-strain domains of the Breaksea Orthogneiss, to metamorphic textures observed in higher-strain domains is inferred to have occurred during deformation, recrystallisation and metamorphism at the grain-scale. Strain localisation into the relatively weaker clinopyroxene and plagioclase domains (Wang et al., 2012; Zhang et al., 2006) partially protected igneous orthopyroxene and some omphacite in cluster interiors. Omphacite recrystallisation and re-equilibration in the omphacite–orthopyroxene granulite reinforce an intimate relationship between metamorphic equilibration and strain intensity that appears at both microscopic- and mesoscopic-scales throughout the Breaksea Orthogneiss, with igneous proportions greater in the lower-strain domains (*e.g.* cluster interiors, eclogite, garnetite and clinopyroxenite pods). However, this variability in strain hinders a simple pluton-scale quantitative assessment of the aggregate of preserved relicts within individual rock components, but estimates of ferromagnesian phases in omphacite–orthopyroxene granulite suggest 10–20%. A more wide-ranging quantification, additionally involving feldspars, however requires further investigation.

7.2. Magmatic protolith histories: fractionation and accumulation

Clinopyroxene in omphacite–orthopyroxene granulite has higher total REE content and slightly lower jadeite contents compared to clinopyroxene in omphacite–garnet granulite. In addition, rare igneous garnet in omphacite–orthopyroxene granulite is generally more HREE enriched than igneous Type 1 grains in the common omphacite–garnet granulite body. Apatite modal proportions within both components are low, implicating a relatively minor influence on the (L)REE budget (Clarke et al., 2013). The higher total HREE content in omphacite and garnet from omphacite–orthopyroxene granulite is consistent with their protolith formation prior to the garnet monzodiorite during a period of limited garnet crystallisation, although the nearly identical whole-rock REE contents reflect a cognate relationship between causal magmas (Table 1). Our preferred interpretation is that the orthopyroxene-bearing granulite and eclogite protoliths reflect early-fractionated components of the Breaksea Orthogneiss magma(s) (*e.g.* Kelley and Cottrell,

Table 3
Summary of interpreted igneous and metamorphic growth stages in ferromagnesian phases.

Lithology	Phase	Microstructural occurrence	Igneous growth stage	Metamorphic growth stage(s)
Omphacite–orthopyroxene granulite	Opx	Cluster centre	High-Al cores	Rims
	Omp	Cluster centre	Lower-Jd cores	Rims
	Omp	Cluster tails		Higher-Jd
	Grt_1	Cluster centre	HREE-enriched cores	HREE-depleted rims
Reaction zones	Grt_2	Coronae		HREE-depleted
	Omp	Adjacent to Grt		Higher-Jd
	Opx	Cluster centre	Disequilibrium	HREE-depleted rims

2012), on the basis of elevated heavy-REE in garnet, and ferric iron in orthopyroxene, omphacite, ulvöspinel and rare Type 1 garnet (Fig. 6). Assuming that all the mineral phases are igneous in origin, then the variation in oxide minerals between orthopyroxene and garnet monzodiorite suggests a variation in fO_2 between the two sequences (Lattard et al., 2005; Luth and Canil, 1993). Although a significant uncertainty exists in ferric iron estimates based on charge balance, systematic differences are maintained in the ferric iron end-member contents of phases between the two sequences (core compositions) outside of the analytical uncertainty (Fig. 6). Alone these estimates are indefinite, however together with distinct oxide phase stability they support qualitatively higher fO_2 inferences (*e.g.* Canil and O'Neill, 1996).

All the rock components of the Breaksea Orthogneiss have similarities in the major and trace element compositions of constituent minerals consistent with their origin from a single magma series (the Western Fiordland Orthogneiss). The liquidus growth of garnet (Clarke et al., 2013) and its high partitioning of the REE compared to other mineral phases, means that the HREE content of garnet can be used as a proxy for crystallisation timing. This study has identified that some of the most HREE-enriched garnet grains occur as rare grains co-existing with unusually HREE-enriched omphacite in omphacite–orthopyroxene granulite, interpreted as the earliest crystallised component of the Breaksea Orthogneiss. Together these two phases controlled the majority of the HREE budget, in the absence of high proportions of accessory phases such as zircon (*e.g.* Rubatto, 2002). This rock also has the most oxidised assemblage and mineral chemistry. The ulvöspinel-bearing crystallisation sequence is interpreted to have occurred prior to rutile-bearing garnetite, clinopyroxenite, and eclogite together recording parts of a progressive fractionation cycle, based on decreasing garnet HREE content and clinopyroxene proportions (Clarke et al., 2013). In addition, the negative Eu anomaly of hypersthene, garnet and omphacite in orthopyroxene eclogite from Breaksea Sound is consistent with the parent magma of that rock being distinct to that responsible for the omphacite–orthopyroxene granulite, it having stabilised with plagioclase, remnants occurring as inclusions, and higher proportions of garnet. These relationships are consistent with the intrusion, fractionation and recrystallisation of several magma pulses in a high-*P* lower arc environment.

The absence of garnet and the presence of orthopyroxene in igneous assemblages is primarily controlled by pressure, temperature and composition (Green, 1972, 1982). However, evidence for *P*–*T* differences in rocks forming the Breaksea Tops would be contrived: orthopyroxene monzodiorite occurs as inclusions within garnet monzodiorite, both of which contain high-*P* igneous clinopyroxene. Higher fO_2 and associated Mg# ($Mg/Mg + Fe^{2+}$) in a magma has been shown to enhance the stability of orthopyroxene and suppress garnet nucleation at high-*P* (~2.0 GPa: Allen and Boettcher, 1978, 1983; Day et al., 1992). In association with the preferential stabilisation of ilmenite up-pressure at higher fO_2 (Sission et al., 2005) it is likely that fO_2 has impacted garnet crystallisation in some early formed parts of the Breaksea Orthogneiss. The presence of minor igneous Type 1 garnet in orthopyroxene monzodiorite is consistent with suppressed nucleation. Instead clinopyroxene is predicted as the main crystallisation phase near the liquidus for a high fO_2 monzodiorite, based on the observed high HREE and elevated ferric iron content in the omphacite–orthopyroxene granulite. Orthopyroxene is inferred to have stabilised with, or prior to garnet, based on garnet and omphacite inclusions and low HREE content in orthopyroxene-bearing eclogite and granulite. Quartz inclusions are restricted to orthopyroxene in granulite, consistent with continuous growth enclosing late crystallising quartz during the final stages of melt solidification (*e.g.* Flood and Vernon, 1988). On this basis the early crystallisation sequence is interpreted to be omphacite–orthopyroxene–garnet–plagioclase–ulvöspinel/magnetite–apatite–quartz prior to the garnet monzodiorite sequence (garnet–omphacite–plagioclase–rutile: Clarke et al., 2013). Progressive crystallisation resulted in subtle decreases in Fe and Mg mineral content from the orthopyroxene-bearing cumulate to the parent. On the premise of the observed outcrop, cumulus proportions from orthopyroxene monzodiorite are minor (<5%) and significantly less than the volumetrically greater garnet monzodiorite (up to 30%: Clarke et al., 2013).

8. Conclusions

The Breaksea Orthogneiss includes two chemically similar granulite components: (1) garnet monzodiorite recrystallised to omphacite–garnet granulite, which has inclusions of (2) orthopyroxene monzodiorite recrystallised to omphacite–orthopyroxene granulite. Preserved crystal facets in orthopyroxene in omphacite–orthopyroxene granulite and omphacite porphyroclasts surrounded by recrystallised grains are consistent with a relic igneous assemblage partially overprinted by tectonometamorphic assemblages and microstructures. Orthopyroxene in this omphacite–orthopyroxene granulite has REE patterns and major element content similar to orthopyroxene in orthopyroxene eclogite reflecting common igneous precursors and variable accumulation of phenocrysts from related magmas. Omphacite and rare igneous garnet in omphacite–orthopyroxene granulite have higher total REE contents compared with omphacite and garnet in omphacite–garnet granulite and eclogite. These relationships are consistent with the high-*P* (1.8–2.0 GPa) igneous crystallisation of omphacite and orthopyroxene with limited igneous garnet. Early, more oxidised magma is interpreted to have initially crystallised orthopyroxene and ulvöspinel, suppressing garnet crystallisation at high-*P*. The fractionation of oxygen into early crystallising phases (ulvöspinel, magnetite, orthopyroxene and ferric iron-rich omphacite) drove the magma to less oxidising conditions, resulting in the more voluminous igneous assemblage of garnet, omphacite and rutile.

Supplementary data to this article can be found online at http://dx.doi.org/10.1016/j.lithos.2014.11.019.

Acknowledgements

TC was supported by an Australian Postgraduate Award from the University of Sydney and AR by a University of Sydney International Scholarship. Logistical and analytical funding was provided by the Discovery Project (DP120102060 to SP and NRD), Future Fellowship (FT1101100070 to SP) and internal funding from the School of Geosciences, University of Sydney. We thank the Department of Conservation in Te Anau for permission to visit and sample localities within Breaksea Sound, Fiordland National Park. The analytical data were obtained using instrumentation funded by DEST Systemic Infrastructure

Grants, ARC LIEF, NCRIS, industry partners and Macquarie University. M. Scambelluri and two anonymous reviews are thanked for comments and editorial handling. This is contribution 523 from the ARC Centre of Excellence for Core to Crust Fluid Systems (http://www.ccfs.mq.edu.au) and 969 in the GEMOC Key Centre (http://www.gemoc.mq.edu.au).

References

Allen, J.C., Boettcher, A.L., 1978. Amphiboles in andesites and basalt: II. Stability as a function of P–T–fH_2O–fO_2. American Mineralogist 63, 1074–1087.

Allen, J.C., Boettcher, A.L., 1983. The stability of amphibole in andesite and basalt at high-pressure. American Mineralogist 68, 307–314.

Allibone, A.H., Tulloch, A.J., 2004. Geology of the plutonic basement rocks of Stewart Island, New Zealand. New Zealand Journal of Geology and Geophysics 47, 233–256.

Allibone, A.H., Jongens, R., Turnbull, I.M., Milan, L.A., Daczko, N.R., De Paoli, M.C., Tulloch, A.J., 2009. Plutonic rocks of Western Fiordland, New Zealand: field relations, geochemistry, correlation, and nomenclature. New Zealand Journal of Geology and Geophysics 52, 379–415.

Behn, M.D., Keleman, P.B., 2006. Stability of arc lower crust: insights from the Talkeetna arc section, south central Alaska, and the seismic structure of modern arcs. Journal of Geophysical Research 111, 1–20.

Beltka, P.M., Klepeis, K.A., 2013. Three-stage evolution of lower crustal gneiss domes at Breaksea Entrance, Fiordland, New Zealand. Tectonics 32, 1084–1106.

Bohlen, S.R., Essene, E.J., 1978. Igneous pyroxenes from metamorphosed anorthosite massifs. Contributions to Mineralogy and Petrology 65, 433–442.

Bradshaw, J.Y., 1989. Origin and metamorphic history of an Early Cretaceous polybaric granulite terrain, Fiordland, southwest New Zealand. Contributions to Mineralogy and Petrology 103, 346–360.

Bradshaw, J.D., 1993. A review of the Median Tectonic Zone: terrane boundaries and terrane amalgamation near the Median Tectonic Line. New Zealand Journal of Geology and Geophysics 36, 117–125.

Canil, D., O'Neill, H., 1996. Distribution of ferric iron in some upper-mantle assemblages. Journal of Petrology 37, 609–635.

Clarke, G.L., Klepeis, K.A., Daczko, N.R., 2000. Cretaceous high-P granulites at Milford Sound, New Zealand: metamorphic history and emplacement in a convergent margin setting. Journal of Metamorphic Geology 18, 359–374.

Clarke, G.L., Daczko, N.R., Miescher, D., 2013. Identifying relic igneous garnet and clinopyroxene in eclogite and granulite, Breaksea Orthogneiss, New Zealand. Journal of Petrology 54, 1921–1938.

Daczko, N.R., Halpin, J.A., 2009. Evidence for melt migration enhancing recrystallization of metastable assemblages in mafic lower crust, Fiordland, New Zealand. Journal of Metamorphic Geology 27, 167–185.

Daczko, N.R., Milan, L.A., Halpin, J.A., 2009. Metastable persistence of pelitic metamorphic assemblages at the root of a Cretaceous magmatic arc — Fiordland, New Zealand. Journal of Metamorphic Geology 27, 233–247.

Daczko, N.R., Emani, S., Allibone, A.H., Turnbull, I.M., 2012. Petrogenesis and geochemical characterisation of ultramafic cumulate rocks from Hawes Head, Fiordland, New Zealand. New Zealand Journal of Geology and Geophysics 55, 361–374.

Day, R.A., Green, T.H., Smith, I.E.M., 1992. The origin and significance of garnet phenocrysts and garnet-bearing xenoliths in Miocene calc-alkaline volcanics from Northland, New Zealand. Journal of Petrology 33, 125–161.

De Paoli, M.C., Clarke, G.L., Klepeis, K.A., Allibone, A.H., Turnbull, I.M., 2009. The eclogite–granulite transition: mafic and intermediate assemblages at Breaksea Sound, New Zealand. Journal of Petrology 50, 2307–2343.

De Paoli, M.C., Clarke, G.L., Daczko, N.R., 2012. Mineral equilibria modeling of the granulite–eclogite transition: effects of whole-rock composition on metamorphic facies type-assemblages. Journal of Petrology 53, 949–970.

DeBari, S.M., Coleman, R.G., 1989. Examination of the deep levels of an island arc: evidence from the Tonsina ultramafic–mafic assemblage, Tonsina, Alaska. Journal of Geophysical Research 94, 4373–4391.

Droop, G.T.R., 1987. A general equation for estimating Fe^{3+} concentrations in ferromagnesian silicates and oxides from microprobe analyses, using stoichiometric criteria. Mineralogical Magazine 51, 431–435.

Flood, R.H., Vernon, R.H., 1988. Microstructural evidence of orders of crystallization in granitoid rocks. Lithos 21, 237–245.

Green, T.H., 1970. High pressure experimental studies on the mineralogical constitution of the lower crust. Physics of the Earth and Planetary Interiors 3, 441–450.

Green, T.H., 1972. Crystallization of calc-alkaline andesite under controlled high-pressure hydrous conditions. Contributions to Mineralogy and Petrology 34, 150–166.

Green, T.H., 1982. Anatexis of mafic crust and high pressure crystallization of andesite. In: Thorpe, R.S. (Ed.), Andesites: Orogenic Andesites and Related Rocks. John Wiley and Sons, Chichester.

Green, D.H., Ringwood, A.E., 1967. An experimental investigation of the gabbro to eclogite transformation and its petrological applications. Geochimica et Cosmochimica Acta 31, 767–833.

Griffin, W.L., Carswell, D.A., Nixon, P.H., 1979. Lower-crustal granulites and eclogites from Lesotho, Southern Africa. In: Boyd, F.R., Meyer, H.O.A. (Eds.), The Mantle Sample: Inclusions in Kimberlites. American Geophysical Union, Washington, pp. 59–86.

Harley, S.L., 1984. The solubility of alumina in orthopyroxene coexisting with garnet in FeO–MgO–Al_2O_3–SiO_2 and CaO–FeO–MgO–Al_2O_3–SiO_2. Journal of Petrology 25, 665–696.

Holness, M.B., Cheadle, M.J., McKenzie, D., 2005. On the use of changes in dihedral angle to decode late-stage textural evolution in cumulates. Journal of Petrology 46, 1565–1583.

Holness, M.B., Humphreys, C.S., Sides, R., Helz, R.T., Tegner, C., 2012. Toward an understanding of disequilibrium dihedral angles in mafic rocks. Journal of Geophysical Research 117, 1–31.

Indares, A.D., 1993. Eclogitized gabbros from the eastern Grenville Province: textures, metamorphic context, and implications. Canadian Journal of Earth Sciences 30, 159–173.

Jagoutz, O., Schmidt, M.W., 2012. The formation and bulk composition of modern juvenile continental crust: the Kohistan arc. Chemical Geology 298–299, 79–96.

Kelley, K.A., Cottrell, E., 2012. The influence of magmatic differentiation on the oxidation state of Fe in a basaltic arc magma. Earth and Planetary Science Letters 330, 109–121.

Kimbrough, D.L., Tulloch, A.J., Geary, E., Coombs, D.S., Landis, C.A., 1993. Isotopic ages from the Nelson region of South Island New Zealand: crustal structure and definition of the Median Tectonic Zone. Tectonophysics 225, 433–448.

Kimbrough, D.L., Tulloch, A.J., Coombs, D.S., Landis, C.A., Johnston, M.R., Mattinson, J.M., 1994. Uranium–lead zircon ages from the Median Tectonic Zone, New Zealand. New Zealand Journal of Geology and Geophysics 37, 393–419.

Kotková, J., Harley, S.L., 2010. Anatexis during high-pressure crustal metamorphism: evidence from garnet–whole-rock REE relationships and Zircon–Rutile Ti–Zr thermometry in leucogranulites from the Bohemian Massif. Journal of Petrology 51, 1967–2001.

Kretz, R., 1983. Symbols for rock-forming minerals. American Mineralogist 68, 277–279.

Lattard, D., Sauerzapf, U., Käsemann, M., 2005. New calibration data for the Fe–Ti oxide thermo-oxybarometers from experiments in the Fe–Ti–O system at 1 bar, 1000–1300 °C and a large range of oxygen fugacities. Contributions to Mineralogy and Petrology 149, 735–754.

Lund, M.D., Piazolo, S., Harley, S.L., 2006. Ultrahigh temperature deformation microstructures in felsic granulites of the Napier Complex, Antarctica. Tectonophysics 427, 133–151.

Luth, R.W., Canil, D., 1993. Ferric iron in mantle-derived pyroxenes and a new oxybarometer for the mantle. Contributions to Mineralogy and Petrology 113, 236–248.

Middlemost, E.A.K., 1994. Naming materials in the magma/igneous rock system. Earth Science Reviews 37, 215–224.

Morimoto, N., 1989. Nomenclature of pyroxenes. Canadian Mineralogist 27, 143–156.

Mørk, M.B.E., 1985. A gabbro to eclogite transition on Flemsøy, Sunnmøre, Western Norway. Chemical Geology 50, 283–310.

Mortimer, N., Gans, P., Calvert, A., Walker, N., 1999. Geology and thermochronometry of the east edge of the Median Batholith (Median Tectonic Zone): a new perspective on Permian to Cretaceous crustal growth of New Zealand. The Island Arc 8, 404–425.

Muir, R.J., Weaver, S.D., Bradshaw, J.D., Eby, N.D., Evans, J.A., 1995. The Cretaceous Separation Point batholith, New Zealand: granitoid magmas formed by melting of mafic lithosphere. Journal of the Geological Society of London 152, 689–701.

Muir, R.J., Ireland, T.R., Weaver, S.D., Bradshaw, J.D., Evans, J.A., Eby, N.D., Shelley, D., 1998. Geochronology and geochemistry of a Mesozoic magmatic arc system, Fiordland, New Zealand. Journal of the Geological Society of London 155, 1037–1053.

Nakamura, D., 2003. Stability of phengite and biotite in eclogites and characteristics of biotite- or orthopyroxene-bearing eclogites. Contributions to Mineralogy and Petrology 145, 550–567.

Norman, M.D., Griffin, W.L., Pearson, N.J., Garcia, M.O., O'Reilly, S.Y., 1998. Quantitative analysis of trace element abundances in glasses and minerals: a comparison of laser ablation inductively coupled plasma mass spectrometry, solution inductively coupled plasma mass spectrometry, proton microprobe and electron microprobe data. Journal of Analytical Atomic Spectrometry 13, 477–482.

O'Brien, P.J., Rötzler, J., 2003. High-pressure granulites: formation, recovery of peak conditions and implications for tectonics. Journal of Metamorphic Geology 21, 3–20.

Pattison, D.R.M., 2003. Petrogenetic significance of orthopyroxene-free garnet + clinopyroxene + plagioclase ± quartz-bearing metabasites with respect to the amphibolite and granulite facies. Journal of Metamorphic Geology 21, 21–34.

Prior, D.J., Trimby, P.W., Weber, U.D., Dingley, D.J., 1996. Orientation contrast imaging of microstructures in rocks using forescatter detectors in the scanning electron microscope. Mineralogical Magazine 60, 859–869.

Racek, M., Štípská, P., Powell, R., 2008. Garnet–clinopyroxene intermediate granulites in the St. Leonhard massif of the Bohemian Massif: ultrahigh-temperature metamorphism at high pressure or not? Journal of Metamorphic Geology 26, 253–271.

Ringuette, L., Martignole, J., Windley, B.F., 1999. Magmatic crystallization, isobaric cooling, and decompression of the garnet-bearing assemblages of the Jijal sequence (Kohistan terrane, western Himalayas). Geology 27, 139–142.

Rubatto, D., 2002. Zircon trace element geochemistry: partitioning with garnet and the link between U–Pb ages and metamorphism. Chemical Geology 184, 123–138.

Rudnick, R.L., Fountain, D.M., 1995. Nature and composition of the continental crust: a lower crustal perspective. Reviews of Geophysics 33, 267–309.

Sandiford, M., Powell, R., 1986. Pyroxene exsolution in granulites from Fyfe Hills, Enderby Land Antarctica: evidence for 1000 °C metamorphic temperatures in Archean continental crust. American Mineralogist 71, 946–954.

Schröter, F.C., Stevenson, J.A., Daczko, N.R., Clarke, G.L., Pearson, N.J., 2004. Trace element partitioning during high-P partial melting and melt–rock interaction; an example from northern Fiordland, New Zealand. Journal of Metamorphic Geology 22, 443–457.

Sission, T.W., Ratajeski, K., Hankins, W.B., Glazner, A.F., 2005. Voluminous granitic magmas from common basaltic sources. Contributions to Mineralogy and Petrology 148, 635–661.

Štípská, P., Powell, R., 2005. Does ternary feldspar constrain the metamorphic conditions of high-grade meta-igneous rocks? Evidence from orthopyroxene granulites, Bohemian Massif. Journal of Metamorphic Geology 23, 627–647.
Svahnberg, H., Piazolo, S., 2010. The initiation of strain localisation in plagioclase-rich rocks: insights from detailed microstructural analyses. Journal of Structural Geology 32, 1404–1416.
Taylor, S.R., McLennan, S.M., 1985. The Continental Crust: Its Composition and Evolution. Blackwell, Oxford.
Urai, J.L., Means, W.D., Lister, G.S., 1986. Dynamic recrystallisation of minerals. In: Hobbs, B.E., Heard, H.C. (Eds.), Mineral and Rock Deformation (Laboratory Studies). Geophysical Monograph of the American Geophysical Union, pp. 161–200.
Vernon, R.H., 1970. Comparative grain-boundary studies of some basic and ultrabasic granulites, nodules and cumulates. Scottish Journal of Geology 6, 337–351.
Vernon, R.H., 2014. Microstructures of microgranitoid enclaves and the origin of S-type granitoids. Australian Journal of Earth Sciences 61, 227–239.
Vernon, R.H., Collins, W.J., Cook, N.D.J., 2012. Metamorphism and deformation of mafic and felsic rocks in a magma transfer zone, Stewart Island, New Zealand. Journal of Metamorphic Geology 30, 473–488.
Wang, Y.F., Zhang, J.F., Jin, Z.M., Green, H.W., 2012. Mafic granulite rheology: implications for a weak continental lower crust. Earth and Planetary Science Letters 353–354, 99–107.
Williams, M.L., Melis, E.A., Kopf, C.F., Hanmer, S., 2000. Microstructural tectonometamorphic processes and the development of gneissic layering: a mechanism for metamorphic segregation. Journal of Metamorphic Geology 18, 41–57.
Zhang, J., Green, H.W., Bozhilov, K.N., 2006. Rheology of omphacite at high temperature and pressure and significance of its lattice preferred orientations. Earth and Planetary Science Letters 246, 432–443.